Spring 2017

Asymmetric Membranes for High Capacity Lithium-Ion Battery Electrodes

Ian Byrd

ASYMMETRIC MEMBRANES FOR HIGH CAPACITY LITHIUM-ION BATTERY

ELECTRODES

by

IAN C. BYRD

(Under the Direction of Ji Wu)

ABSTRACT

Lithium-Ion Batteries (LIBs) have broad applications such as portable electronic devices, electric vehicles, and for green energy storage from intermittent sources. Current LIBs are limited by their low capacity materials at both the anode and cathode. At the anode, graphite suffers from a low capacity of only 372 mAh g^{-1}. The most commonly used cathode material is $LiCoO_2$ which has a meager capacity of 140 mAh g^{-1}. Thereby the broader applications of LIBs are limited due to these low capacities. It is imperative to develop higher capacity materials to further improve the performance of LIBs. Silicon is an ideal candidate to replace commercial anode materials due to its high theoretical capacity of 4200 mAh g^{-1} and vanadium pentoxide (V_2O_5) is a leading candidate for cathodes with an impressive capacity of 294 mAh g^{-1} when two lithium ions are inserted per V_2O_5 unit. Unfortunately, silicon suffers from an extreme volume expansion of ~300% upon charging. This causes the material to crack leading to permanent capacity loss. V_2O_5 also suffers from some volume expansion issues, but the biggest obstacle to overcome is its low electrical conductivity and ion diffusivity. Herein, we report the fabrication of composite single, double, and triple-layer asymmetric membranes containing micron size silicon as anode materials and single-layer asymmetric membranes containing V_2O_5 as cathode materials. Anodes fabricated with an asymmetric membrane structure demonstrate a capacity of 610 mAh g^{-1} after 100 cycles with an

88% capacity retention at 0.5 C. Cathodes demonstrate a capacity of over 160 mAh g^{-1} with ~100% capacity retention at 0.5 C in 380 cycles. It is found that the choice of conductive additives and annealing temperature can have a significant effect on V_2O_5 particle morphology and cycling performance. Lower annealing temperatures and the addition of conductive graphene are shown to be beneficial to improving cycling performance. This scalable method may provide a universal answer for other anode and cathode materials with volume expansion issues.

KEY WORDS: Lithium-ion batteries, Silicon, Vanadium pentoxide, Asymmetric membranes, High capacity

ASYMMETRIC MEMBRANES FOR HIGH CAPACITY LITHIUM-ION BATTERY

ELECTRODES

by

IAN C. BYRD

B.S., Georgia Southern University, 2011

A Thesis Submitted to the Graduate Faculty of Georgia Southern University in Partial

Fulfillment of the Requirements for the Degree

MASTER OF SCIENCE

STATESBORO, GEORGIA

ASYMMETRIC MEMBRANES FOR HIGH CAPACITY LITHIUM-ION BATTERY

ELECTRODES

by

IAN C. BYRD

Major Professor: Ji Wu
Committee: Donald McLemore
                    Rafael Quirino

Electronic Version Approved:
May 2017

DEDICATION

This thesis is dedicated to my parents, Jeffrey P. Byrd and Lisa A. Byrd, for their unwavering support and showing me the importance of hard work and dedication;

To all of my mentors for challenging me to make the most out of myself at all times;

To my girlfriend, Jade Boykin, who has been with me every step of the way and has supported me throughout this whole project,

For without any of you this would never have been possible.

ACKNOWLEDGEMENTS

I would like to acknowledge Georgia Southern University and the Chemistry Department for allowing the use of their facilities. I would also like to acknowledge the Master of Science in Applied Physical Science program within the College of Graduate Studies at Georgia Southern University for their tuition waiver and graduate teaching assistantship funding. In addition, I would like to recognize both the Graduate Student Organization and the College of Science and Mathematics at Georgia Southern University for their support of my research through research grants I received. I want to thank the Student Government Association and the Graduate Student organization for the funding I received to support travel to conferences to present my research. I want to thank Dr. Ji Wu for all his guidance as I progressed through this master's program. I would also like to thank other students who have helped me in the lab throughout my project including: Ryan Bujol, Tyler Camp, Theron Webber, and Shavonne Lovelace. I want to recognize Kathleen McCormac for all her help when I was an undergraduate getting started in my research journey. Also, I want to thank the faculty at Georgia Southern for their help including Dr. Hao Chen for his help with the SEM-EDS, Dr. Nathan Takas for help with various instruments, and Dr. Don McLemore for help with the TGA. I acknowledge help I received from Dr. Clifford Padgett at Armstrong State University for his assistance with Powder X-Ray Diffraction. Lastly, I would like to acknowledge my collaborators at other institutions such as: Jianlin Li at Oak Ridge National Laboratory and Congrui Jin, Anju Sharma, and Hanlei Zhang at Binghampton University.

TABLE OF CONTENTS

LIST OF TABLES

LIST OF FIGURES

CHAPTER 1: Introduction

1.1. *Brief History of Lithium-Ion Batteries*

Lithium-Ion Batteries (LIBs) were first commercialized by Sony in 1991. The first LIBs consisted of a graphite anode (negative electrode) and a $LiCoO_2$ cathode (positive electrode) with a membrane separator to keep the anode and cathode from touching, as well as a lithium ion conducting electrolyte. This configuration in commercial rechargeable lithium ion batteries has remained largely unchanged since its invention.[1] During charging, lithium ions are inserted into the anode while simultaneously being extracted from the cathode without causing any permanent structural changes. LIBs possess many advantages over other traditional types of batteries such as lead acid or alkaline batteries. One leading advantage is its higher energy density over most other types of batteries. Commercial LIBs can have a specific energy of up to 120-150 W h kg^{-1}, which is much greater than that of lead acid batteries (20-40 W h kg^{-1}).[2] This much improved energy density allows for a battery to supply the same amount of energy with a significantly smaller mass. Likewise, a battery of the same mass will deliver a much greater amount of energy (Figure 1).
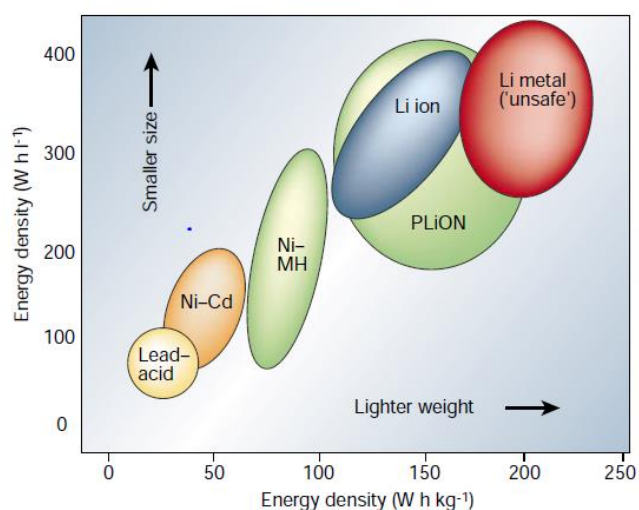
Figure 1: Comparison of energy density per kg and per L of different types of battery systems. Reprinted with permission from reference 2. Copyright 2001, Nature Publishing Group.

1.2.   Applications of Lithium-Ion Batteries

LIBs have a wide range of applications from electric vehicles to portable electronic devices and even large scale energy storage from intermittent energy sources such as solar and wind power.[3] Currently, the largest market for LIBs is the portable electronics sector. However, in the future the electric vehicle market is expected to experience the biggest expansion by the year 2020.[4] The demand for electric vehicles will likely continue to increase as fossil fuels are non-renewable and may cause many social, health, environmental and climate detriments, thus forcing society to look for a greener alternative to the internal combustion engine in automobiles. Consequently, the total market for LIBs is projected to reach $46.21 billion by 2022.[4] Another use for LIBs is in energy storage for intermittent power sources such as solar and wind power.[5] In these applications, batteries are used to store the energy generated so that it can be used at a later time. It is reported by the Department of Energy (DOE) that the pumped hydroelectricity accounts for 95% (23.4 GW) of this energy storage (Figure 2). The other 5% is stored via thermal storage (36%, 431 MW), compressed air (35%, 423 MW), batteries (26%, 304 MW), and flywheels (3%, 40 MW).[6] If LIB capacity and performance can be improved significantly without cost increase, there is a great potential to store large amounts of energy in a small area, thus giving them an advantage over the currently dominating hydroelectric energy storage.
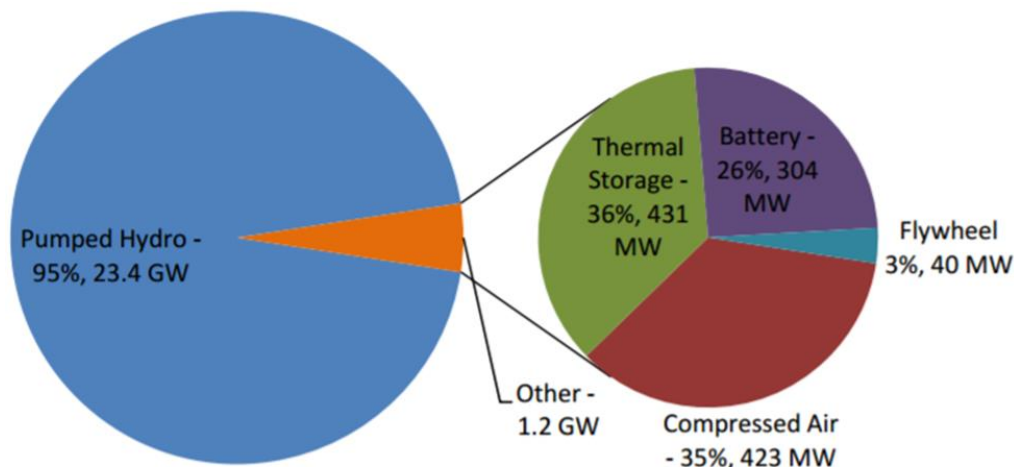
Figure 2: Pie charts comparing the current methods for grid energy storage.[6]

1.3. *How Does a Lithium Ion Battery Function?*

A rechargeable (secondary) LIB has three main components: an anode (negative electrode), a cathode (positive electrode), and a separator membrane to keep the battery from short circuiting. There is also a Li-ion conducting electrolyte dissolved in organic solvents such as ethylene carbonate, diethyl carbonate, and dimethyl carbonate. The most common lithium salt used as the electrolyte is $LiPF_6$. The anode and cathode materials are cast onto a current collector. At the anode, the current collector is usually made of copper thin film while aluminum foil is commonly employed as the cathode current collector. In a full cell battery, the lithium source is at the cathode. When a battery is being charged, the Li-ions migrate from the cathode to the anode. At this point, the cathode is being oxidized and undergoes the following electrochemical reaction:

$$LiCoO_2 \rightarrow Li_{1-x}CoO_2 + xLi^+ + xe^- \text{(half-cell potential: 1 V)}^7$$
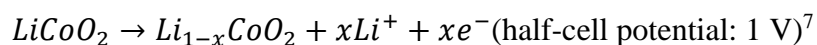
When the cathode is being oxidized, the anode is simultaneously undergoing a reduction as shown by the following reaction:

$$C_6 + xLi^+ + xe^- \rightarrow C_6Li_x \text{ (half-cell potential: ~-3V)}^7$$
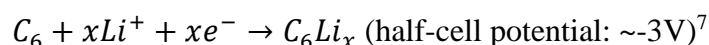
Both of these reactions combined gives the overall redox reaction in a LIB[8]:

$$LiCoO_2 + C_6 \leftrightarrow C_6Li + CoO_2 \text{ (full-cell potential: 4 V)}^{[7]}$$
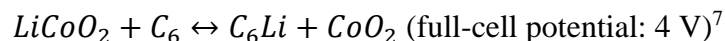
It is notable that all the half-cell potentials shown above are relative to standard hydrogen electrode (SHE). The general schematic for the function of a LIB is seen in Figure 3.[9] This figure shows LiFePO4 as the cathode material, but the general function is still the same as a LiCoO2 cathode.[1] When Li-ions are released from the solid matrix of the cathode, the electrons flow through an external circuit creating a current flow to the anode. When the Li-ions reach the anode, they can be inserted between graphite sheets which have an interlayer spacing of 3.35 Å. It takes six carbon atoms to hold one Li-ion which corresponds to a capacity of 372 mAh g^{-1}.[10] Upon discharging the reactions are flipped. Oxidation occurs at the anode and results in the release of lithium ions. These lithium ions can migrate towards the cathode under the internal electrical field and are eventually intercalated into the crystal structure of the cathode material.
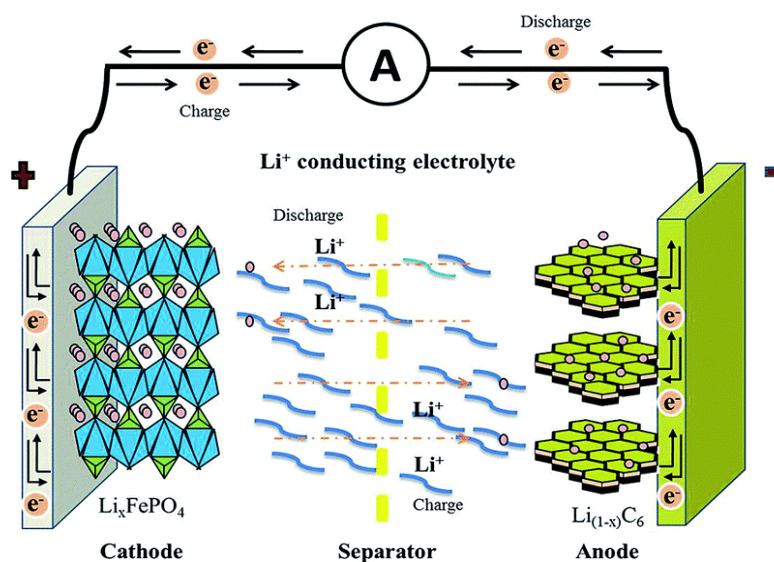
Figure 3: A general schematic demonstrating the charging and discharging processes in a typical LIB cell. Reprinted with permission from reference 9. Copyright 2014, Royal Society of Chemistry.

1.4.   Advantages and Limitations of Current Rechargeable Lithium Ion Batteries

LIBs are superior to other types of rechargeable batteries in a few ways. The major advantage is energy density. Energy density can be defined as the amount of energy stored per unit volume or per unit mass. LIBs have a specific energy of 120-150 W h kg^{-1} which is roughly two to three times greater than Nickel-Cadmium batteries.[2] This higher specific energy allows for more energy to be stored in a smaller area which is especially desirable for electric vehicles and portable electronic devices. Another major benefit of LIBs is their high operating voltage. The operating voltage of a full cell LIB is equal to the electrode potential of the cathode minus the electrode potential of the anode.[11] A typical LIB has an operating voltage of up to 4.0 V. Compared to the voltage of Nickel-Metal Hydride and Nickel-Metal Cadmium batteries (1.2 V), LIBs deliver a voltage over three times greater.[12] This means it would take three Nickel-Metal Hydride batteries connected together to deliver the same voltage as only one LIB does. In other words, LIBs have a much higher power output than their Nickel counterparts.

There are also a few drawbacks to using LIBs. The major concern regarding the use of LIBs is safety. Flammability of the $LiPF_6$ electrolyte dissolved in an organic solvent is one of the main concerns for LIB safety.[13] Aside from the flammable solvent, LIBs are also very sensitive to high temperatures. They are not very efficient at dissipating heat. The potential range of 4 V in LIBs is much greater than the thermodynamic stability window for both anode and cathode materials.[14] When a battery is being charged and discharged, there are some exothermic side reactions that occur between the anode, cathode, and electrolyte. These reactions result in a temperature increase inside the cell. This increase in temperature then causes the reaction rates to increase and thus creating an even higher temperature. This phenomenon is known as thermal runaway.[15] Once this process begins, there is little that can be done to stop it. The overall

temperature of a cell is determined by the heat balance between the amount of heat lost and the amount of heat dissipated. If a cell cannot effectively dissipate heat, then thermal runaway is set to occur.[16] Thermal runaway is especially dangerous in electric vehicles and plug in hybrids because they utilize large amount of smaller cells connected together in circuit. Thermal runaway in one battery cell can release enough heat to cause neighboring cells to reach a temperature at which thermal runaway can occur.[17]

In addition to safety concerns, current LIBs suffer from a relatively low capacity. In order for electric vehicles to replace traditional internal combustion engine vehicles, the range of electric vehicles needs to be vastly improved. As mentioned above, most commercial LIBs use graphite anode and $LiCoO_2$ cathode. Although graphite is a very stable material that can be cycled thousands of times with minimal capacity fade, it suffers from an intrinsically low capacity of 372 mAh g^{-1} that is not enough to meet the demand of future all-electric vehicles as reported by DOE.[3, 18-20] Graphite is ideal because Li-ions can insert into graphite's layered structure with little volume expansion and minimum internal stress. To satisfy the requirements for use in electric vehicles, other materials with much higher capacities need to be investigated for use in LIBs.

In addition to improving the capacity of the anode material, the cathode side cannot be overlooked. In order for a LIB to function properly the ratio between the capacity of the anode and the capacity of the cathode must be properly balanced. For LIBs the ideal capacity ratio of cathode to anode is 1.1 to 1 to prevent lithium plating at the anode.[21] The relatively low cathode capacity will become a much bigger issue if the anode material is increased well above the current capacity in commercial LIBs, i.e., the adoption of high capacity silicon anodes. In order to balance the capacity, a much larger mass of cathode material must be added to match the anode. This can be done by increasing the thickness of the active material loading on cathode current collector sheets

or making the cathode current collector much larger in area. Both designs have negative outcomes in the overall electrochemical performance of the cell. If the electrode area is increased, the overall size of the battery will not be any smaller, thus lowering the overall areal energy density of the entire cell. If the thickness is too large, there will be a huge detrimental effect on the overall rate capability, lithium ion diffusion, and the overall lifespan of the cell itself.[22] It has been shown that thicker electrodes show lower power density as well as a faster capacity fade.[22-23] Jie Liu and his collaborators conducted an experiment in which they compared the performance of full cell LIBs using two different cells, one cell with thick electrodes and another with thin electrodes. Their results back up their hypothesis and show that in cells with thick electrodes the temperature of the cell is much higher than that of the cell with thin electrodes. They attribute the higher temperature to the increased internal resistance of the cell as the result of the increased electrode thickness. As previously mentioned, the temperature increase may cause a battery to reach thermal runaway and greatly decrease the overall safety of the cell.[23]

1.5.   Silicon as Anode Material for Second-Generation High Capacity Lithium-Ion Batteries

There are a few other alternatives to using graphite as the anode material in LIBs. One of those is to use germanium powder. Germanium is attractive because of its high theoretical capacity (1600 mAh g^{-1}).[18, 24] It also is much higher in conductivity than silicon and has a greater mechanical strength. However, there are still extreme volume expansion issues to overcome and germanium is much more expensive than silicon.[18] Another promising alternative is tin dioxide (SnO_2). SnO_2 has a theoretical capacity of 790 mAh g^{-1} but suffers from similar volume expansion issues.[25] In addition to volume expansion, SnO_2 also has a huge irreversible capacity loss in the first cycle due to the formation of highly insulating Li_2O, which is widely deemed as an electrochemically non-

recyclable compound in LIBs. This consumes large amounts of lithium, further limiting its practical use in LIBs.[26]

Silicon (Si) is a leading candidate to replace traditional graphite anodes due to its theoretical capacity of 4200 mAh g^{-1} based on the fully lithiated form of Si_5Li_{22}.[3, 20, 27-29] However, even though Si has a capacity over eleven times higher than graphite, it suffers from a massive volume change of roughly 300% upon lithiation/de-lithiation.[30] This volume expansion causes Si particles to crack because it will generate extremely large electrode stress and Si has a poor mechanical strength. As a result, the electrode may peel away from the current collector leading to a permanent capacity loss in only a few cycles.[31] In order for Si to replace graphite, the extreme volume expansion needs to be tamed. One of the most common methods to alleviating the trouble of volume expansion is to use nanoscale composite materials. The majority of research in literature on Si involves some sort of nanostructuring to allow Si to expand without losing capacity. These nanostructures include nanoparticles (NPs), nanowires (NWs), nanotubes (NTs), nano-thin films, as well as mesoporous and macroporous materials.[3, 21, 32-33] Nanomaterials are widely used due to their unique physical and chemical properties. In the case of Si, nanoparticles are much more resistant to cracking because at small enough dimensions the mechanical strength of Si is improved to the point where cracking will no longer occur upon lithiation/de-lithiation.[27] In addition, nano-sized Si particles are much more conductive than their micron-size counterparts due in large part to the decreased lithium-ion diffusion length and diffusion barrier. This is especially important considering lithium ions have a much smaller diffusion coefficient in silicon than in graphite ($\sim 10^{-10}$ vs. 10^{-6} cm^2 s^{-1}).[3, 31]

Wang et al. fabricated a binder-free three-dimensional silicon/carbon nanowire networks for high performance lithium-ion battery anodes via a wet etching method and chemical vapor

deposition (CVD) of carbon on the surface of the Si NWs. Once the Si NWs were fabricated, they were immersed in an ethanol solution and sonicated to adequately disperse them in solution. Si NWs were then allowed to precipitate into a thin film of Si NWs. The ethanol was evaporated and carbon was coated on the Si NWs via CVD. This creates the free-standing Si NW/C film used directly as a binder free anode material. The group was able to achieve an initial capacity of nearly 2500 mAh g^{-1}, but the capacity is reduced to below 1500 mAh g^{-1} in 30 cycles. Even though the capacity retention is poor, they are able to show that longer Si NWs can retain their capacity much better in 30 cycles. The group also milled some of their wires into shorter lengths. The results show that shorter wires have poorer electrochemical performance which is attributed to the lack of continuous electron transport pathways.[34]

Yang et al. designed a creative yolk-shell silicon-mesoporous anode material. This yolk shell structure was formed by a multistep fabrication process that allows for a single Si NP to be encapsulated inside a mesoporous carbon shell with free space inside for Si to expand and contract without being leached out into the electrolyte. They were able to create 50 nm of free space between the outer shell and the Si NP embedded within. This unique structure leads to an impressive cycling performance (Figure 4). These yolk-shell structures were able to maintain a capacity of around 1000 mAh g^{-1} for 400 cycles with little capacity loss. Though the capacity is much lower than the theoretical value of 4200 mAh g^{-1}, the stability is impressive. Although the stability is impressive, creating the free space needed requires dangerous chemicals and difficult processes thus lowering its commercial feasibility.[32]
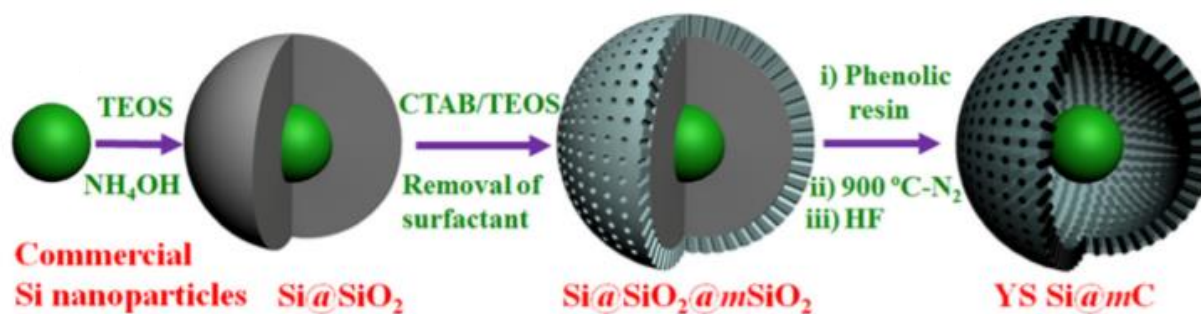
Figure 4: Outline of the synthesis of yolk-shell silicon encapsulated in mesoporous carbon coatings. Reprinted with permission from reference 32. Copyright 2015, Elsevier.

There is significantly less research being conducted in the realm of micron-size Si than for nano-Si. One of the main benefits for using Si micron particles (Si MPs) is cost. In order to commercialize Si electrodes, the cost must be comparable to current LIB anodes. Currently, Si NPs are around one order of magnitude more expensive than Si MPs.[3, 35] This low cost makes Si MPs much more economically feasible if the drawbacks in their performance can be overcome. Along with cost, there are other benefits of using Si MPs over Si NPs such as these larger particles having a much higher tap density.[29, 36]

Yi Cui's group at Stanford is one of few groups attempting to tackle the challenges that come with using Si MPs. His group has fabricated self-healing conductive polymers with low glass transition temperatures (T_g) to replace traditional polymer binders used in commercial LIBs. Their self-healing polymer allows for Si to expand and contract while still being held in good contact with conductive additives as well as the current collector (Figure 5). The low T_g of the polymer allows it to have elastomeric properties at room temperatures. Electrodes fabricated from these self-healing polymers and Si MPs have an impressive initial capacity of around 2500 mAh g^{-1} as well as 80% capacity retention in 90 cycles. Their data shows that their self-healing polymer binder

is superior to current commercial binders, however their capacity is steadily decreasing over the course of 120 cycles and needs to be improved for practical use.[29]
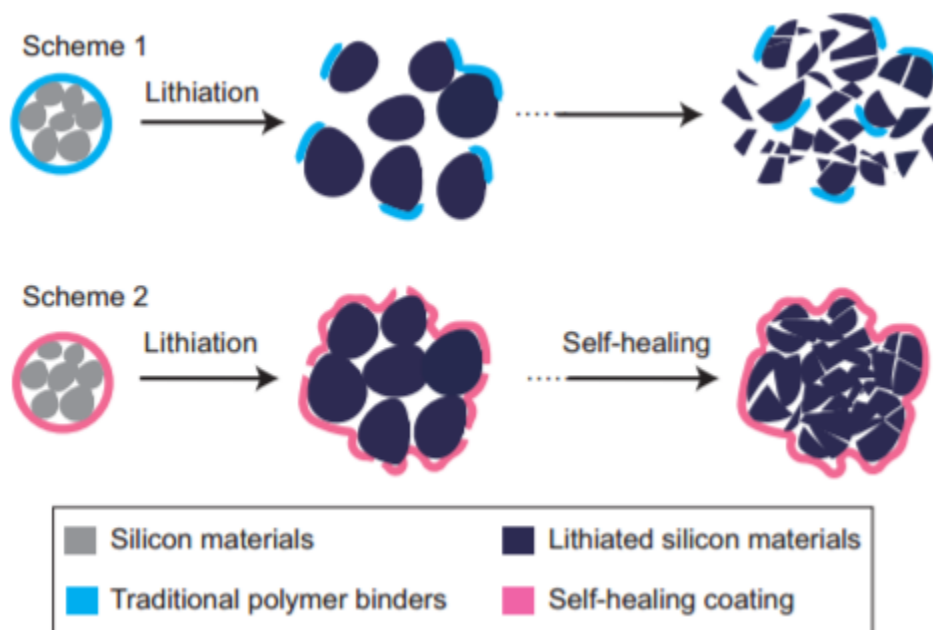
Figure 5: Comparison of traditional polymer binders to self-healing binders fabricated by Cui's group. Reprinted with permission from reference 29. Copyright 2013, Nature Publishing Group.

Cui's group also published a paper using a mechanical pressing method and micron sized Si. This study is unique in that the authors state that they can produce large quantities of product (>20 g) with 95% yield. This leads them to conclude that their method is highly scalable. They produce Si MPs by starting with silica coated silicon nanospheres and using high pressure to press them into bulk sized pellets. These pellets were then ball milled to create particles with an average size of around 4.5 µm. Once the milling process is complete the particles were heated to 600°C for 2 hours to bridge neighboring particles together and ensure that they do not break off into smaller particles later on. Once the particles were heated they were then carbon coated and acid etched with HF to remove SiO_2, creating void space for the Si MPs (Figure 6). They are able to

reach an initial capacity of 1250 mAh g^{-1}, 95% of which is retained after 1400 cycles at a charging

rate of 1C. These results are compatible with what is needed for commercial batteries. However,

both the silica and carbon coating processes require CVD which requires high temperatures and

expensive precursor gases. Also, the etching process involves using HF, which is the most

dangerous and corrosive acid, further hindering its potential for large scale production.[36]
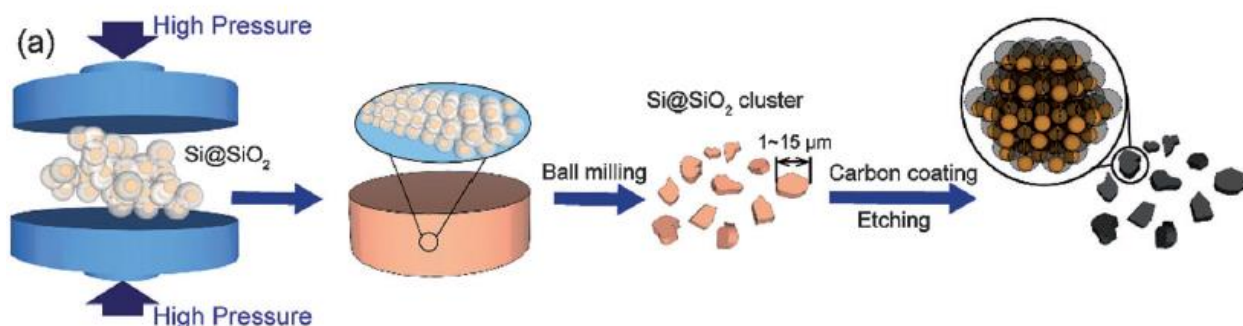
Figure 6: Schematic diagram for the fabrication of Si MPs via the mechanical pressing of nano-Si@SiO$_2$ clusters, ball milling into micron-size particles, and carbon coating with acid etching to remove SiO$_2$. Reprinted with permission from reference 36. Copyright 2015, Royal Society of Chemistry.

Gao Liu's group at the Lawrence Berkeley National Laboratory is also working with

micron size Si. Their method involves an in situ formed network of Si MPs and Si NPs using a

highly cross-linked conductive polymer binder. The idea is that they use the Si NPs as an additional

conductive additive in the place of traditional conductive additives and make use of a polymer that

is much more resistant to strain, particularly non-recoverable deformation. Even though a high

capacity of over 3000 mAh g^{-1} is achieved, there is only a 73% capacity retention after only 30

cycles. The capacity retention needs to be significantly improved in order to meet the needs of

commercial batteries.[37]

1.6.   Vanadium Pentoxide as a High Capacity Cathode for Lithium-Ion Batteries

Extensive work is being done to improve cathode capacity by using alternative high capacity and low cost materials. $LiCoO_2$ is the most commonly used cathode but suffers from a low capacity (140 mAh g^{-1}) and is costly to produce. The material with the highest capacity at the cathode for LIBs is sulfur that has a theoretical capacity of 1672 mAh g^{-1}.[38] Sulfur is also cheap to produce and is environmentally benign. However, sulfur has an extremely low electrical conductivity and the dissolution of polysulfides in electrolytes can reduce its cycle life rapidly.[39] There have been very few reports of high capacity cathodes using sulfur that have decent capacity retention over repeated cycling. There are other materials with lower capacities but much higher cyclability than sulfur that could be used. One of the leading candidates is $LiNiO_2$. $LiNiO_2$ is both lower in cost and higher in capacity than $LiCoO_2$.[40] Although it has some advantages, there are also some limiting factors. The $LiNiO_2$ structure is less ordered than $LiCoO_2$ which causes Ni to occupy some of the lithium sites and thus limits lithium ion diffusion.[41]

Vanadium Pentoxide (V_2O_5) is an attractive candidate to replace current commercial cathodes in LIBs because of its high theoretical capacity of 294 mAh g^{-1} when two lithium ions are intercalated into the layered structure of V_2O_5.[42-43] This is much higher than the capacity for current commercial cathode materials ($LiCoO_2$: 140 mAh g^{-1}; $LiMn_2O_4$: 148 mAh g^{-1}; $LiFePO_4$: 170 mAh g^{-1}).[42] Although V_2O_5 has a high capacity, it falls short in a few key categories. The charging rate capability of bulk V_2O_5 is severely limited due to its low electron conductivity and lithium ion diffusivity.[44] Along with the low conductivity, V_2O_5 also experiences some volume expansion issues similar to those seen with silicon at the anode. Recently, a few strategies have been employed to overcome these issues. These include the synthesis of nanoparticles (NPs), nanowires (NWs), and nanobelts (NWs). [43, 45-46] Nanostructurings are ideal for V_2O_5 because the

reduced particle size can increase the ionic conductivity of V_2O_5 by dramatically reducing the diffusion length so that the rate capability is more satisfying.

1.7.   *Vanadium Pentoxide Lithium-Ion Kinetics*

The layered structure of V_2O_5 makes it an attractive alternative to commercial cathode materials. The sheet-like structure of V_2O_5 is shown in Figure 7.[47] A large spacing between the sheets (4.368 Angstroms) allows for facile lithium insertion due to the small atomic radius of lithium (1.67 Angstroms).[48-49] Two lithium-ions can be reversibly inserted into the layered structure of crystalline V_2O_5. It is possible for a third lithium ion to be inserted to reach a theoretical capacity of 440 mAh g^{-1} when discharged to 1.9 V. But the lithium ion cannot be extracted and the battery ceases to cycle.[43, 50] This irreversible process can be avoided by cycling in a voltage window above 1.9 V. The insertion of lithium ions can be explained through a series of reactions that take place upon lithium insertion into crystalline V_2O_5. Lithium insertion gives way to five phases of $Li_xV_2O_5$ (α, ε, δ, γ, ω), the last of which is the non-reversible phase. The initial α phase is formed when 1% of lithium is inserted into V_2O_5 sheets.[48] The ε-phase ($\varepsilon - Li_{0.5}V_2O_5$) is formed when 0.5 Li-ion is inserted into one V_2O_5 unit on average as shown through the following reaction:

$$V_2O_5 + 0.5Li^+ + 0.5e^- \leftrightarrow \varepsilon - \ Li_{0.5}V_2O_5$$
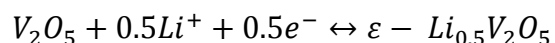
This reaction can be observed at a potential of ~3.4 V. The exact voltage may vary from sample to sample depending on the electrode over-potential and solid electrolyte interphase (SEI) stability. At this point, there is minimal volume expansion that does not affect the reversibility. The next phase formed is the δ-phase ($\delta - LiV_2O_5$) when one Li-ion is inserted and is demonstrated through the following reaction which is commonly observed at a potential of 3.1 V:

$$Li_{0.5}V_2O_5 + 0.5Li^+ + 0.5e^- \leftrightarrow \delta - \ LiV_2O_5$$
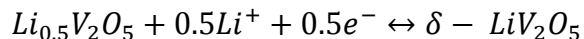
This is the last fully reversible phase where V_2O_5 can be fully de-lithiated back to its original pristine V_2O_5 form. At this point the reactions still do not affect the strong V-O bond. If insertion is halted at this phase, the reversible capacity would be 147 mAh g^{-1}, which is comparable to commercial cathodes. However, commercial cathodes have much more satisfying capacity retention over the course of many cycles.[51] Once more than 1 lithium is inserted a transition to the γ-phase ($\gamma - Li_2V_2O_5$) will occur when the second lithium ion is inserted.[48] The corresponding chemical reaction is shown below:

$$LiV_2O_5 + Li^+ + e^- \leftrightarrow \gamma - Li_2V_2O_5$$
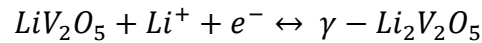
The final transition occurs at a potential of ~2.3 V and corresponds to a reversible capacity of 294 mAh g^{-1}. After this transition, the layered crystal structure starts to be puckered and generate internal lattice strain, potentially leading to irreversible capacity loss if there is no extra protection. As previously mentioned there is another phase that can be formed when V_2O_5 is cycled to potentials below 1.9 V. This phase is called ω-phase ($\omega - Li_3V_2O_5$) corresponding to the third lithium insertion. This phase has a rock-salt cubic structure as opposed to the original orthorhombic structure for $\alpha - V_2O_5$.[52] This phase is also non-reversible because the lithium diffusion coefficient is reduced from 3.3 x 10^{-9} cm^2 s^{-1} when 2 lithium ions are inserted to 10^{-12} cm^2 s^{-1} when a third lithium ion is inserted.[48] The reaction for this transition is as follows:

$$Li_2V_2O_5 + Li^+ + e^- \rightarrow \omega - Li_3V_2O_5$$
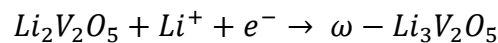
Upon de-lithiation, the reactions will happen in reverse order starting from the γ-phase back to the α-phase and each phase corresponds to a potential of 2.2, 3.1, and 3.3 V, respectively.[48, 53]
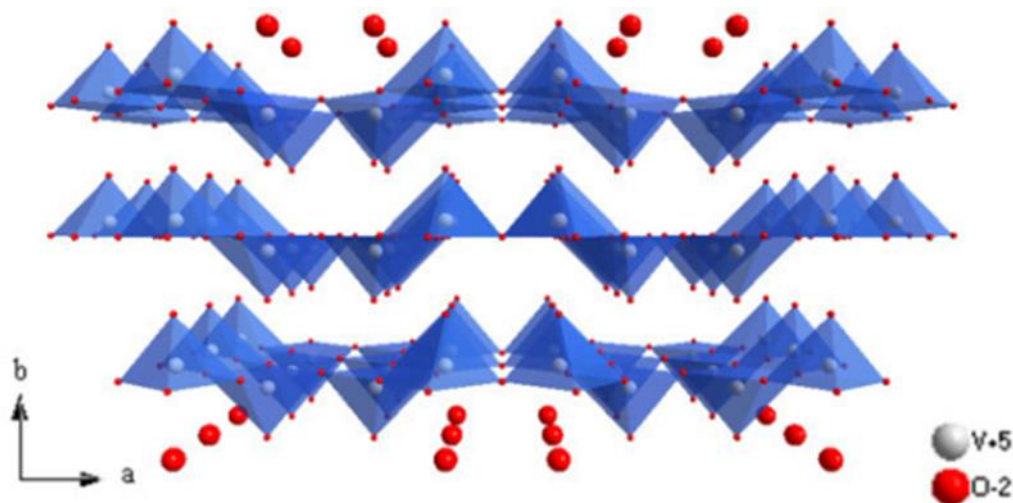
Figure 7: Layered structure of V_2O_5. Note: the weak V-O bond is not shown in this diagram. Reprinted with permission from reference 47.

1.8.   Current Research Status of Vanadium Pentoxide Lithium-Ion Battery Cathode

Yun Xu et al. fabricated a two dimensional V_2O_5 sheet network for use as the cathode material in LIBs. This group also fabricated manganese doped V_2O_5 sheets.[42] It is believed that these carbon coated two-dimensional nanosheets can increase lithium ion diffusion by providing a pathway for the lithium ions. The carbon coating serves the purpose of increasing the electrical conductivity of their 2D sheets, thus increasing its rate capability. The purpose of doping the sheets with manganese is to increase the electrochemical performance and increase electrical conductivity even further. They are able to achieve a capacity based on the mass of V_2O_5 only of over 300 mAh g^{-1} for the first cycle, but the capacity drops dramatically to ~200 mAh g^{-1} in the second cycle. In the first 10 cycles, some capacity is regained but the capacity drops steadily over the course of only 50 cycles. The manganese doped electrodes show improved stability, but suffer from a lower capacity. In order to be used in a commercial battery the stability needs to be greatly improved.[42] Also, the capacity based on total electrode mass should be calculated for a full cell LIB.

James M. Tour's group at Rice University used a similar graphene nanoribbon/ V_2O_5 composite material for use as the cathode in LIBs.[43] They utilize graphene nanoribbons (GNR) to enclose nanocrystalline V_2O_5 particles by "unzipping" multi-walled carbon nanotubes (MWCNTs). The group first fabricated the GNR from unzipped MWCNTs. The MWCNTs were combined with 1,2-dimethoxyethane and a Na/K alloy in a N_2 filled glovebox. The solution was stirred for three days then filtered and dried. Next, the GNRs were combined with 1,2-dimethoxyethane and varying amounts of Na/K alloy under N_2 atmosphere. Then, VCl_4 was added with stirring for two days. This causes V^{4+} to be reduced to V^0 NPs by the Na/K alloy while being intercalated into the GNR. This composite was then annealed at 250°C for 3 hrs to oxidize vanadium to vanadium oxides. The three-dimensional conductive matrix is shown to be able to increase the conductivity and therefore improve the rate performance as well as the stability of V_2O_5 particles. The group is able to attain a high capacity of 278 mAh g^{-1}, but like other studies, this capacity is calculated based on the mass of V_2O_5 alone. Considering that the electrode contains only 40 wt. % V_2O_5 particles, the capacity based on the total electrode mass is calculated to be only 110 mAh g^{-1} considering that carbon does not have any contribution to capacity at a voltage window of 2 – 4 V. The capacity retention rate is also unsatisfying at only 78% in 100 cycles (Figure 8). Although their structure shows an increased performance over V_2O_5 particles alone, the overall capacity based on total electrode mass needs to be improved as well as the capacity retention rate.[43]
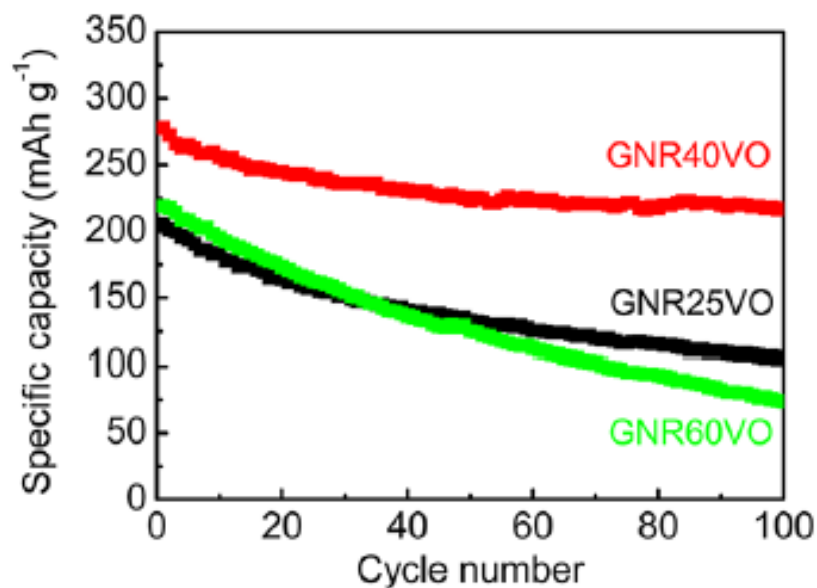
Figure 8: Cycling performance of different mass loadings of V_2O_5. Reprinted with permission from reference 43. Copyright 2014, American Chemical Society.

1.9.   Brief History of Asymmetric Membranes and Their Formation Mechanisms

Asymmetric membranes are widely used in water filtration and water desalination due to their unique asymmetric porous structure consisting of a network of nanopores and macropores. This structure allows a high water flux while also being able to reject salts and other larger macromolecules.[54] These membranes are produced almost exclusively through immersion precipitation where the membrane forms through a process called phase inversion.[55] They can be produced on a large scale via a roll to roll method.

The precipitation process is the main method to producing asymmetric membranes. In this method there are three components: polymer, solvent, and nonsolvent. The membrane is ultimately formed by a process known as phase inversion.[56] Phase inversion can be illustrated through a ternary phase diagram (Figure 9). Each corner of the phase diagram represents a different phase. At any point inside the triangle, all phases are present at different concentrations. The general

procedure for phase inversion requires a polymer to be dissolved into the solvent. Once the polymer is dissolved it is cast onto a substrate to be immersed into the nonsolvent in which the polymer is insoluble. Then, two phases are to be formed, polymer-rich and polymer-lean, resulting in the spontaneous formation of asymmetric membranes. [54, 57]
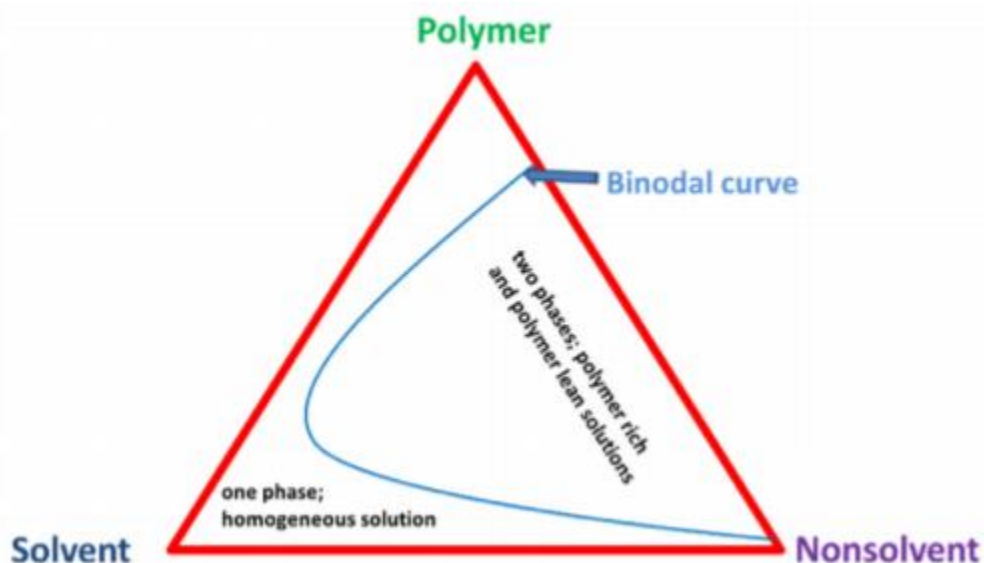
Figure 9: Ternary phase diagram for the phase inversion process.

In general, there are two types of membranes that can be formed, finger-like and a porous sponge structure.[54] Each type of membrane is formed under different precipitation conditions. The rate at which the polymer precipitates is the determining factor for which type of membrane will form. The best way to control the rate of precipitation is by the use of different solvents.[58] Some solvents have a tendency to produce finger-like structures while others produce sponge-like membranes (Figure 10). Finger-like membranes will have a dense skin layer on their surface and a much less dense finger-like network of larger pores underneath. This structure is produced because the skin layer meets the nonsolvent first and is therefore precipitated out of solution faster. At this point the polymeric solution absorbs the nonsolvent quickly and is therefore supersaturated

with polymer and is precipitated from a large number of nucleation sites.[59] This dense skin layer impedes the flow of nonsolvent and therefore causes the underlying layer to have fewer nucleation sites and be precipitated out of solution much more slowly.[54]
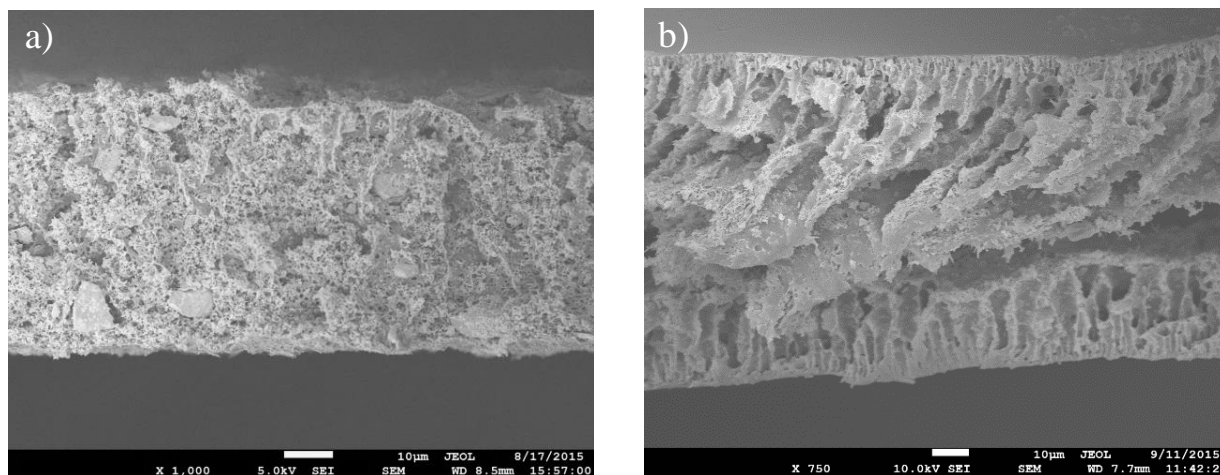
Figure 10: a) An example of a sponge-like polysulfone membrane that was precipitated in ethanol, and b) an example of a membrane polysulfone membrane that was precipitated in DI water.

1.10.   *Our Proposed Hypothesis and General Experimental Design*

It is hypothesized by us that the asymmetric structure consisting of dense nanopores and large macropores can provide an ideal solution to solving the large volume expansion issue of high capacity lithium-ion battery electrodes such as silicon and vanadium pentoxide. The large macropores can provide free space for Si to expand while the dense nanoporous skin layer can prevent cracked Si from being leached out into the electrolyte, causing permanent capacity loss. These membranes can be produced on a large scale via a simple roll to roll method, thus benefiting their potential commercialization.

To adapt these membranes to contain silicon for use as the anode material we will simply add Si MP and a conductive carbon black additive to the polymeric solution and carry out the

phase inversion process in water to generate a fingerlike structure. In order to further stabilize the electrode, either one or both sides of the original membrane will be coated with carbonaceous cellulose acetate membranes. This may help to prevent particles from being leached out into the electrolyte causing permanent capacity loss. These membranes will be carbonized to make them conductive enough for use in LIBs, then glued to a current collector and assembled into coin cell batteries for various electrochemical tests such as cyclability, voltage profiles, electrochemical impedance spectroscopy, rate performance, etc.

For cathode materials, the process is a little different by introducing sol-gel chemistry. We will dissolve a V_2O_5 organometallic precursor in the polymeric solution and then add either carbon black or graphene as a conductive additive. It is hypothesized that graphene may wrap around the V_2O_5 particles, increasing the conductivity greatly. With the addition of an organometallic precursor, the membrane will still form via phase inversion but will be complicated due to the V_2O_5 sol-gel chemistry. Overall, it is predicted that this will not significantly affect the ternary phase diagram and structure of the membrane. These membranes will be carbonized in an inert atmosphere and then annealed in air. The extra annealing step is necessary to oxidize vanadium back to the V_2O_5 form as other charge states of vanadium are not suitable for use in LIBs. Similar to the anode, the membranes will then be glued to a current collector and assembled into half cell batteries for electrochemical tests.

CHAPTER 2: Asymmetric Membranes Containing Micron Size Silicon as Anode Material for

High Capacity Lithium Ion Batteries

2.1.   Introduction

Aforementioned in the introduction, current LIBs are limited by their low capacity graphite anodes with a theoretical capacity of only 372 mAh g^{-1}. An alternative is to incorporate silicon into batteries as a high capacity anode material. Silicon benefits from a high theoretical capacity of 4200 mAh g^{-1} based on the fully lithiated phase of $Si_{22}Li_5$.[3, 17] Unfortunately, with this large capacity comes some serious obstacles to overcome. The biggest issue with silicon is its volume expansion upon cycling. When silicon is lithiated, it can expand up to 300%.[29] Due to the low mechanical strength of silicon, this expansion can cause silicon particles to crack and be peeled away from the current collector, resulting in permanent capacity loss in only a few cycles. In micron-size silicon, these issues are amplified since silicon will continue to crack until it reaches a small enough diameter where the mechanical strength is improved.[60] Most attempts to circumvent this issue involve the use of nano-sized silicon particles.[19, 32-34, 61] However, these nano-sized silicon particles are much more expensive than their micron-size counterparts. Cost is one of the major hindrances to nano-sized silicon being commercially used in LIBs. To overcome this issue, low cost composites with free space to allow for silicon to expand but still maintain good contact with the current collectors are needed.

The asymmetric structure is an ideal structure to contain silicon's volume expansion issues. The dense skin layer on the surface of the membrane can act as a barrier to keep cracked silicon particles trapped inside while the large macropores allow ample space for silicon to expand upon lithiation. These membranes are also produced via a facile phase inversion process.[58-59] Herein, we simply add silicon micron particles (Si MPs) to a polymeric solution and fabricate these

membranes via phase inversion. In addition, it was determined the performance of a single-layer membrane alone was not satisfying (~40% capacity loss in 100 cycles), therefore double-layer and triple-layer (sandwich) membrane coatings were added with no silicon to increase the cycle life. We are able to demonstrate that these additional coatings can stabilize Si MP-based electrodes during cycling.

2.2. Experimental

2.2.1. Synthesis of single-layer asymmetric membranes containing micron-size silicon

First, 0.75 g of polyacrylonitrile (PAN) (M_n=150,000; Pfaltz & Bauer) was dissolved in 11 mL N-methyl-2-pyrrolidone (NMP) (Sigma Aldrich, >99.5%) using a sonic bath (Bransonic CPX3800H) for 1 hr. Next, 0.25 g of as-received Si powder (American Elements, ~1 µm, Figure 13) and 0.20 g carbon black (CB, TIMCAL SUPER C45 with a surface area of 45 m^2 g^{-1}) were added to the solution and dispersed using a sonic bath for 2 hrs. After sonication, the homogenous solution was then coated onto a silicon (100) wafer (2 in. diameter) using a doctor blade set to deliver a wet coating thickness of 100 µm. Next, the coated wafer was immersed in deionized water for phase inversion. The membrane was left in DI water for 30 minutes and then placed in ethanol for another 30 minutes to remove residual moisture. It is noteworthy that the moisture may lead to the oxidation of silicon powders at high temperature during the carbonization process. Finally, the membrane was carbonized at 800°C for 2 hrs in a tube furnace (Lindberg/Blue M™ 1100°C) and under the protection of helium gas (99.9999%, Airgas He UHP300) with a flow rate of 200 sccm. The temperature was ramped at a rate of ~60°C min^{-1}. These membranes are labeled PAN/Si herein.

2.2.2. Synthesis of double-layer asymmetric membranes containing micron-size silicon

A mixture of 0.75 g of cellulose acetate propionate (M_n=15,000; Acros) and 0.2 g of carbon black was dispersed in 5 mL of acetone using a sonic bath for 1 hr. This mixture was then coated on the top of the un-carbonized PAN/Si membrane using a doctor blade set to ~25 µm. Next, the coated membrane was placed into ice cold ether (ACS Grade, EMD Millipore Corporation) for phase inversion to generate a double-layer asymmetric membrane. Lastly, the membrane was carbonized at 800°C for 2 hrs in a tube furnace and labeled as CA/PAN/Si herein.

2.2.3. Synthesis of triple-layer sandwich asymmetric membranes containing micron-size silicon

First, 1.2 g of cellulose acetate and 0.4 g carbon black were dispersed in 15 mL acetone to make a suspension. Next, an un-carbonized PAN/Si asymmetric membrane was dipped directly into the suspension and then slowly withdrawn out of the suspension. In the next step, the dip-coated membrane was immersed into ice cold ether to form a triple-layer sandwich asymmetric membrane. Similarly, the triple-layer sandwich asymmetric membrane was carbonized at 800°C for 2 hrs in a tube furnace and labeled CA/PAN/Si/CA. The synthesis of these membranes is demonstrated in Figure 11.

2.2.4. Synthesis of asymmetric membranes without silicon for control

Asymmetric membranes containing no Si MPs were also prepared using the aforementioned method for control experiments. The membranes were carbonized at 800°C for 2 hours and labeled as PAN.
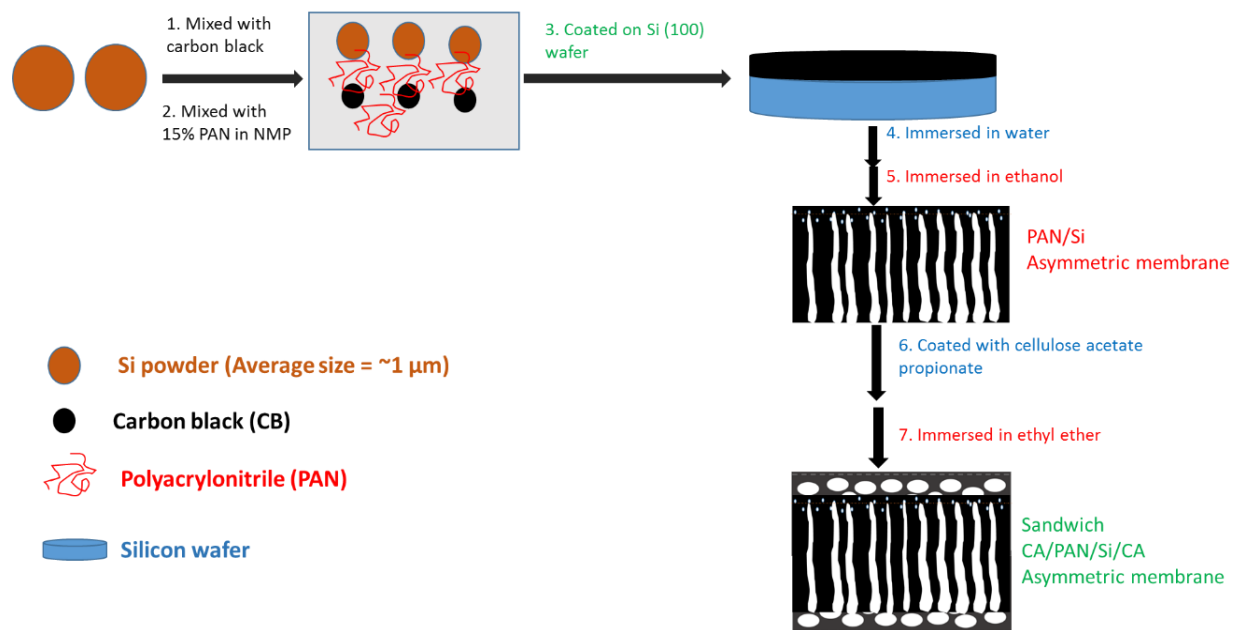
Figure 11: General experimental design for the synthesis of CA/PAN/Si/CA asymmetric membranes.

2.2.5. Characterization

A field emission scanning electron microscope (JEOL JSM-7600F) equipped with a transmission electron detector (TED) was used for morphology and structure characterizations. Raman studies were carried out using a ThermoScientific DXR SmartRaman Spectrometer with a 10x lens magnification, 150 second collection time, a 1 mW laser with a wavelength of 532 nm, and a 50 µm slit aperture. Phase identification was performed using a powder X-ray diffractometer (Rigaku MiniFlex 600) at Armstrong State University. The samples were scanned using Cu K_α (λ=0.1542 nm) radiation with a step rate of 0.2° per second from 10-90° (2Θ). The silicon content was determined using a thermogravimetric analyzer (TA Instruments G50 TGA). Compressed air (Ultra Zero, Airgas) was used as the purging gas with a flow rate of 20 mL min^{-1}. The temperature was ramped from room temperature to 700°C at a rate of 10°C min^{-1}. Surface area and pore size

distribution experiments were completed on a Micrometrics ASAP 2020 Surface Area and Porosity Analyzer. The surface area was calculated using Brunauer-Emmett-Teller (BET) equation and pore size distribution was determined using the Barrett-Joyner-Halenda (BJH) method. Samples were degassed at 50 µTorr and 300°C for 30 minutes. Nitrogen adsorption and desorption was carried out at 77 K using ultra high purity nitrogen gas (Airgas UHP300, 99.9999%).

2.2.6. *Electrode preparation and electrochemical analysis*

Asymmetric membranes were glued to a copper current collector (15 mm diameter, 11 µm thickness; MTI Corporation) using a suspension made of 0.15 g carbon black and 0.15 g of polyacrylic acid (PAA; Aldrich) in 4 mL of ethanol to make the electrodes. Electrodes were then dried in an oven at 100°C for at least 4 hrs to remove residual moisture and ethanol. In the next step, these dried electrodes were assembled into 2032 coin cells (MTI Corporation) using Li metal as the counter electrode and 60 µL electrolyte consisting of 1 M $LiPF_6$ dissolved in ethylene carbonate (EC), dimethyl carbonate (DMC), and diethyl carbonate (DEC) with a 1:1:1 v/v ratio (MTI Corporation). A polypropylene/polyethylene membrane with pore size of 0.21 x 0.05 µm (MTI Corporation) was used as separator. The mass loading of the silicon asymmetric membrane is 1-2 mg per coin cell. The contents of silicon are determined by TGA analysis, which are 46.0 wt.%, 39.6 wt.% and 33.6 wt.% in single-layer, double-layer and triple-layer asymmetric membranes, respectively.

For Si MP coin cell batteries (control sample), 80 wt.% Si MPs, 10 wt.% PAA and 10 wt.% carbon black were sonicated for 2 hrs to create a homogenous slurry. The slurry was coated onto a copper foil using a doctor blade with a wet coating thickness of 100 µm. After being dried, the foil was punched into 15 mm diameter disks and then assembled into coin cells using the same method as mentioned above. The whole battery assembly was carried out in an argon filled glove

box (LCPW, LC Technology Solutions, Inc.) with both oxygen and water content <1 ppm. Galvanostatic cycling of the LIBs was carried out on a Bio-Logic VMP3 multi-channel potentiostat with a voltage window of 0.01-1.50 V vs. Li$^+$/Li. Three formation cycles at a current density of 100 mA g^{-1} were carried out on all coin cell batteries before any other electrochemical tests. Electrochemical impedance spectroscopy (EIS) measurements were carried out in the frequency range of 0.1 Hz – 1 MHz with an amplitude of 10 mV. The data were fitted using an equivalent circuit as shown in Figure 12. R$_s$ stands for the contact resistance; R$_{SEI}$ and C$_{SEI}$ are corresponding to the resistance and capacitance from SEI layer; R$_{ct}$ and C$_{dl}$ represent the charge transfer resistance and double-layer capacitance of the membrane electrode; W$_d$ is the Warburg diffusion impedance.
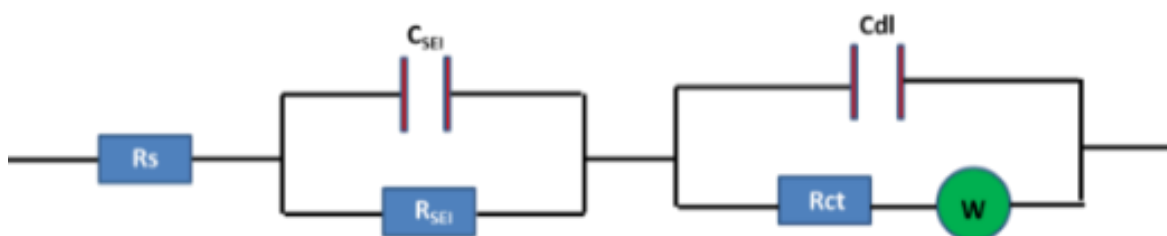
Figure 12: Equivalent circuit used to fit EIS measurements.

2.3.   Results and Discussion

2.3.1.   Characterization

Because Si MPs have irregular shapes, the Heywood diameter ($d_p = 2\sqrt{\frac{A}{\pi}}$) is used to represent the size of these particles, where A is the area of the particle determined from TEM images using ImageJ software (Figure 13a). The average diameter of Si MPs for this study was calculated to be ~1.01 µm (Figure 13b) with a standard deviation of ~0.60 µm, which is highly consistent with the corresponding SEM and TEM images (Figure 13a, 13c and 13d).
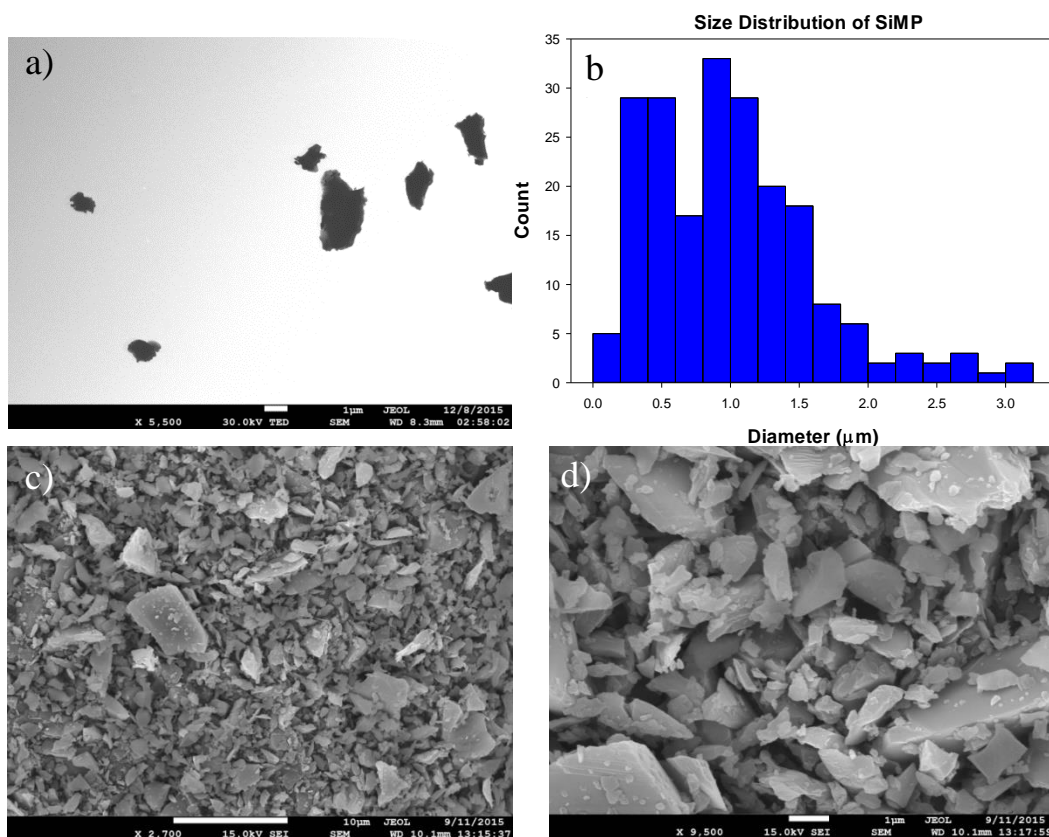
Figure 13: Electron microscope characterization of Si MPs used for this study: a) transmission electron microscope (TEM) image used to calculate size distribution via the ; b) size distribution; c) and d) scanning electron microscope (SEM) images at different magnifications. Note: the scale bars in a) and d) are 1 µm, while the bar in c) represents 10 µm.

Cross-section images of single layer PAN/Si membranes reveal the unique asymmetric structure is present with large macro-pores ~10 µm wide sandwiched between two dense skin layers. It can be seen that the membrane thickness decreased from the original wet coating thickness of 100 µm to ~80 µm. This is caused by solvent de-mixing (Figure 14a). After carbonization, it can clearly be seen that the asymmetric structure is maintained even with the loss of organic material and the thickness is further reduced to ~65 µm (Figure 14d). To further improve the electrochemical stability of the single-layer asymmetric membrane electrode, a cellulose acetate/carbon black solution was coated on one side or both sides of the original single-layer

PAN/Si membrane that was then carbonized to generate double-layer or triple-layer (sandwich) asymmetric membranes (Figure 14b,c,e,f). These carbonaceous membranes are dense sponge-like membranes that serve the purpose of protecting any Si MP that may have precipitated onto the membrane surface during phase inversion. The high-resolution SEM image (Figure 15) shows that the junction between the top carbonaceous layer derived from the carbonized cellulose acetate and the bottom PAN/Si layer is nearly seamless, which is beneficial to an efficient electron transfer across the boundary.
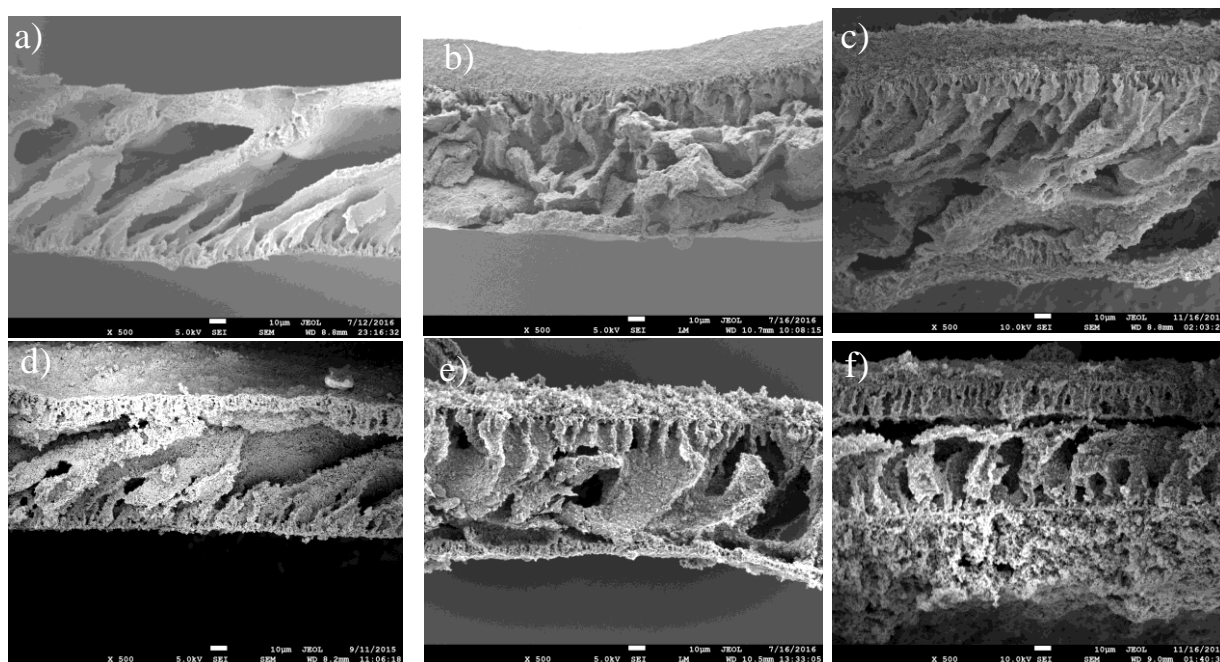
Figure 14: a) PAN/Si single-layer asymmetric membrane before carbonization; b) CA/PAN/Si double-layer asymmetric membrane before carbonization; c) CA/PAN/Si/CA triple-layer asymmetric membrane before carbonization; d) PAN/Si membrane after carbonization at 800°C for 2 hrs; e) CA/PAN/Si membrane after carbonization at 800°C for 2 hrs; f) CA/PAN/Si/CA membrane after carbonization at 800°C for 2 hrs.
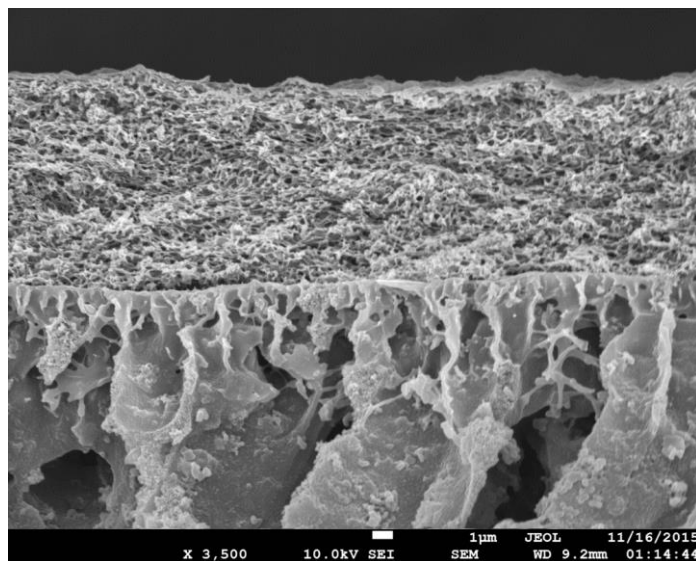
Figure 15: High resolution scanning electron microscope image of the interface in double-layer asymmetric membrane containing Si MPs.

In order to confirm the presence of silicon, Raman Spectroscopy was employed. Raman data shows a sharp peak around 520 cm^{-1} for all samples containing Si MPs, confirming the presence of cubic Si (Figure 16a).[62] For all carbonized membrane samples a weak graphite (1600 cm^{-1}) and defect (1365 cm^{-1}) peak can be clearly distinguished. From this it can be determined that the during the carbonization process a small amount of poorly ordered graphite can be formed. With increasing weight percentages of carbon, the peaks intensify. The phase identification is further confirmed in Figure 16b. In each sample that contains Si, characteristic patterns from cubic phase Si (111), (220), (311), (400), (331) and (422) crystal planes were observed (JCPDS-ICDD No. 27-1402). A broad pattern at 26° can be seen from all types of membranes, which can be ascribed to carbon materials with a poor crystallinity similar to the Raman spectra.[18, 63-64] This peak also increases in intensity as higher weight percentages of carbon are added.
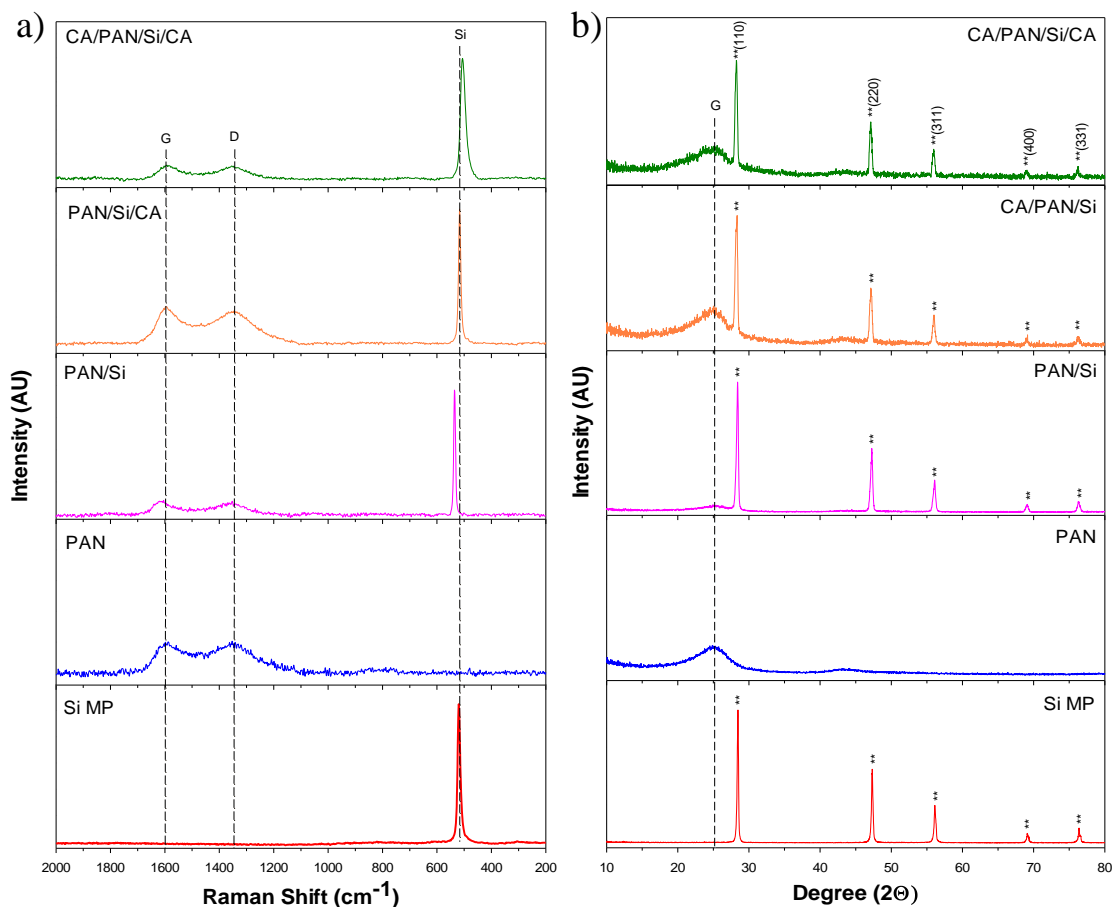
Figure 16: a) Raman spectra of all carbonized membranes and as received SiMP; b) PXRD diffraction patterns of all carbonized membranes and as received SiMP (Note: **: Si, G: graphite).

The silicon content in asymmetric membranes was determined using a Thermogravimetric Analyzer (TGA) under the assumption that carbon can be fully oxidized into CO_2 gas and Si is only slightly oxidized under our TGA conditions. This hypothesis is confirmed by the PAN control membrane which showed a 99.7% weight loss (Figure 17b). Under the same TGA analytical conditions, the mass of pure Si MPs is only slightly increased by less than 1.0%, confirming that Si cannot be significantly oxidized below 700° C in air (Figure 17a). Under this assumption, the content of Si in PAN/Si single-layer, CA/PAN/Si double-layer and CA/PAN/Si/CA triple-layer (sandwich) membranes are 46.0 wt.%, 39.6 wt.% and 33.6 wt.%, respectively (Figure 17c-e). The

gradual decrease in Si content from the single-layer to the triple-layer asymmetric membrane is due to the addition of carbonaceous coatings that do not contain any Si particles.
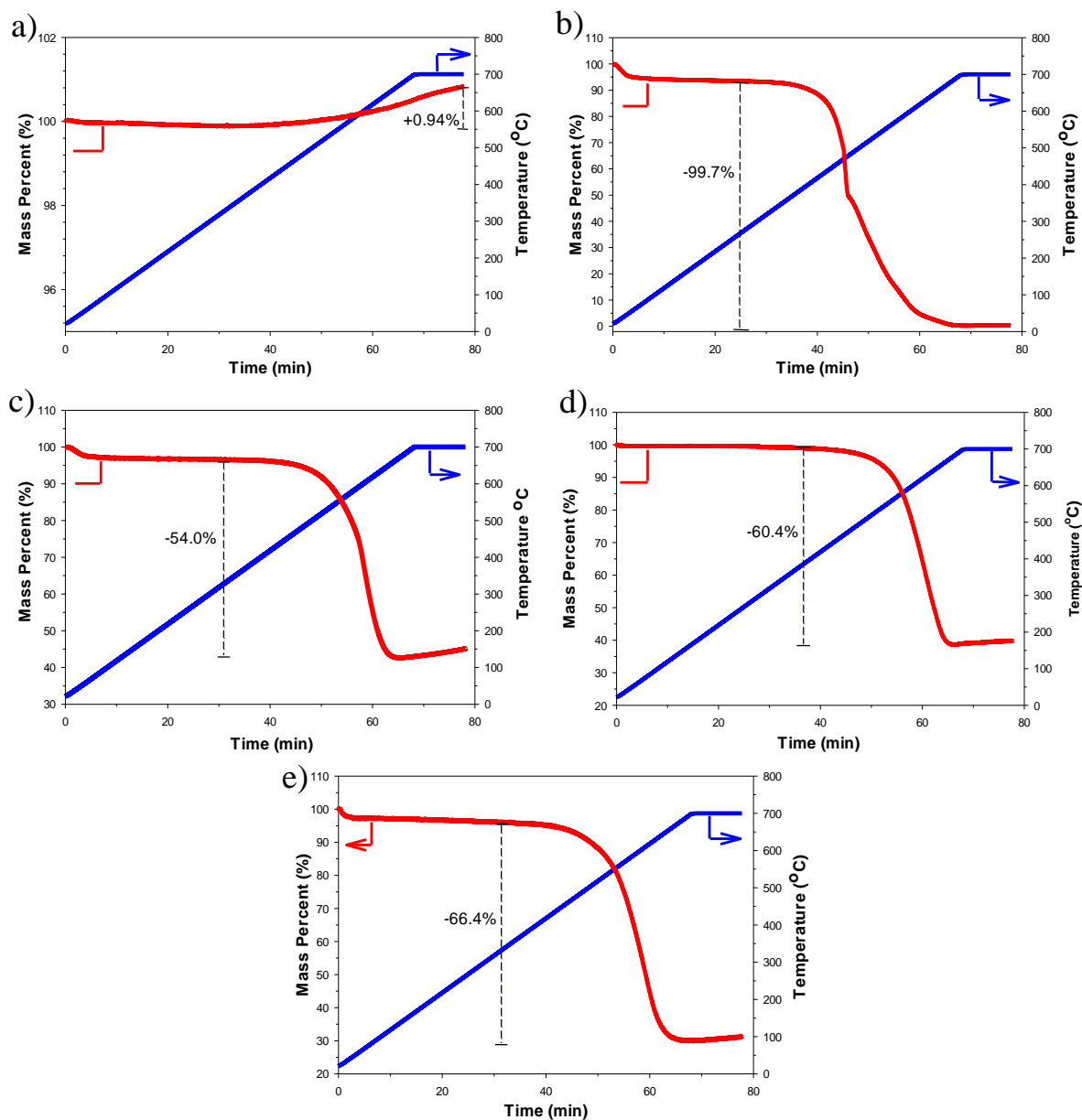
Figure 17: Thermogravimetric analysis of: a) as received SiMP; b) carbonized PAN/CB membrane with no Si added; c) carbonized PAN/Si single membrane; d) carbonized CA/PAN/Si double layer membrane; e) carbonized CA/PAN/Si/CA triple layer membrane.

The BET and BJH equations were used to determine the surface area and porosity of carbonized membranes, respectively (Table 1 and Figure 18). The surface area of CA/PAN/Si/CA sandwich asymmetric membrane is 67.4 m^2 g^{-1}. The double-layer CA/PAN/Si membrane has a slightly lower surface area of 59.6 m^2 g^{-1}. Finally, the single PAN/Si membrane has the lowest surface area of 36.4 m^2 g^{-1}. The trend of increased surface area and increasing number of carbon coatings can be attributed to the highly porous structure of the carbonaceous layer (Table 1). The pore size distribution data shows the majority of pores are less than 40 nm in diameter, but there are some larger pores greater than 100 nm (Figure 18b).
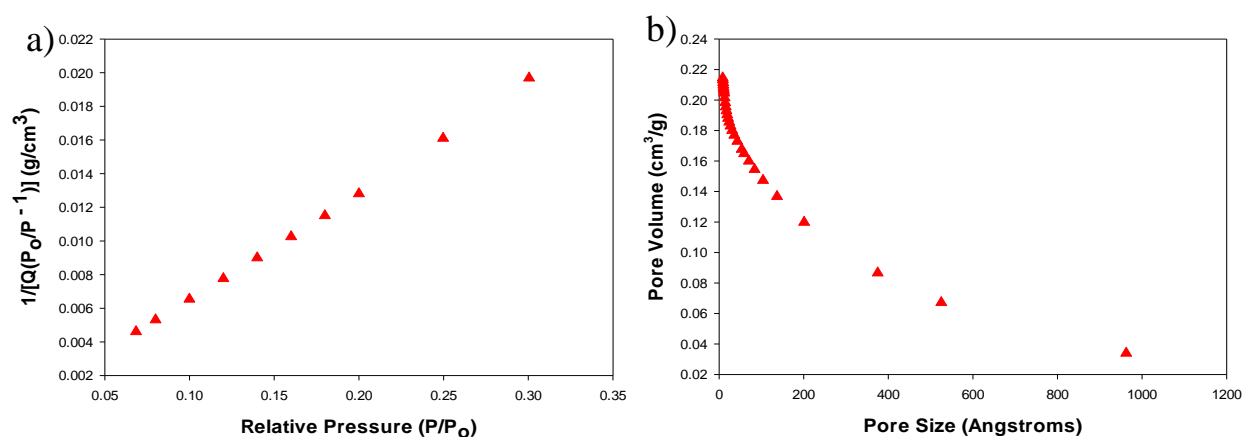
Figure 18: a) surface area plot of CA/PAN/Si/CA triple-layer asymmetric membrane; b) pore size distribution of CA/PAN/Si/CA triple-layer asymmetric membrane.

Table 1: BET surface area of carbonized single-layer, double-layer and triple-layer asymmetric membranes.

Type of membrane	BET specific Area (m^2/g)
CA/PAN/Si/CA; Triple Layer Asymmetric Membrane	67.4
CA/PAN/Si; Double Layer Asymmetric Membrane	59.6
PAN/Si; Single Layer Asymmetric Membrane	36.4

2.3.2. Electrochemical Analysis

The LIBs fabricated using the single layer PAN/Si membrane show a high initial capacity of 968 mAh g^{-1} at a charging rate of 0.5C which corresponds with a two-hour charging and discharging time, respectively (Figure 19b). Unfortunately, the retention is sub-par with only ~40% capacity retention over the course of 100 cycles. Even though the retention is poor, it is a significant improvement over the pure Si MP electrode which experiences nearly 100% capacity loss in as little as five cycles (Figure 19b). This rapid capacity loss is commonly seen in literature.[27, 29, 37] This dramatic increase in cyclability can be credited to the asymmetric porous structure. The structure provides free volume for Si MPs to expand and contract within the large macro-porous network during lithiation/delithiation. However, the nearly 60% capacity loss is not satisfying and needs to be vastly improved. It is believed that the large capacity drop of single-layer PAN/Si membrane may be related to the pulverization of Si MPs on its top surface (Figure 20b). The SEM images of the membrane surface show that after carbonization, many Si MPs become exposed thus can be cracked and leached out into the electrolyte. It is well-known that Si MPs have a high tendency to fracture during lithiation.[60] The fracture of micron-size Si particles can cause loose contact with conductive carbon material.[29] This fracturing will continue until the particle size is small enough to withstand cracking. When this happens, the tiny nanoparticles that are generated may fall into the conductive finger-like channels. This may cause the contact between silicon and carbon to be regained leading to an increase in capacity. This phenomenon may explain why the PAN/Si membrane experiences an initial capacity loss and a full recovery of initially lost capacity up to ~1000 mAh g^{-1}. Additionally, Si NPs can be more efficiently lithiated as compared to Si MPs due to the shortened lithium diffusion length. Even though the capacity is regained initially, after the 20th cycle the membrane is continuously losing active Si particles

without the coating of additional porous carbon coatings on the surface of the PAN/Si single layer membrane.

Based on this assumption that Si MPs on the surface were a major factor in the continuous capacity loss, the single-layer PAN/Si asymmetric membrane was coated with a single-layer or double-layer coating of cellulose acetate (CA) asymmetric membranes to obtain double-layer or triple-layer asymmetric membranes, respectively. The goal of this structuring is to prevent the loss of pulverized silicon particles from the top surface of asymmetric membrane. It is worth noting that the CA asymmetric membrane must be carbonized to make it electrically conductive. Indeed, double-layer CA/PAN/Si asymmetric membrane shows a much improved cyclability as compared to single-layer PAN/Si asymmetric membrane (Figure 19b). Despite an initial capacity loss of ~18% in the first 20 cycles, the capacity remains nearly unchanged from the 20th to 80th cycle. The initial capacity loss may be linked to the pulverization of Si MPs caused by the sudden increase in current after formation cycles are complete. As a result, some Si particles may lose contact with the conductive carbon matrix, thus leading to the capacity loss. The initial capacity of the double-layer CA/PAN/Si asymmetric membrane is 852 mAh g^{-1} at 0.5C. This is slightly lower than that of single-layer membrane and is caused by a lower content of silicon (46.0% in PAN/Si to 39.6% in CA/PAN/Si). The capacity retention of triple-layer CA/PAN/Si/CA asymmetric membrane is far and away superior to other samples (Figure 19a). Over 88% of the initial capacity can be retained after 100 cycles. This impressive retention is seen because the PAN/Si asymmetric membrane is protected by extra porous coatings that can efficiently prevent the loss of pulverized Si particles. The overall capacity of triple-layer asymmetric membrane is 610 mAh g^{-1} at the 100th cycle at a charging rate of 0.5 C. The average coulombic efficiency is 99.8% in 100 cycles (Figure 19a). The coulombic efficiency is the ratio of lithium that is inserted to the amount extracted. It is

especially important in full cell batteries where there is a limited lithium source. Compared to traditional graphite anodes (372 mAh g^{-1}), the triple-layer membranes have a 64% higher capacity. The specific capacity of Si in triple-layer asymmetric membrane was calculated to be ~1447 mAh g^{-1} at 0.5C, assuming the capacity of carbon in the asymmetric membrane is ~340 mAh g^{-1} based on the capacity for the PAN membrane alone (Figure 19a). This capacity is significantly below the theoretical value for silicon because of the relatively fast charging rate. At high charging rates, it is difficult for silicon to be fully lithiated. In addition, it has been reported that at room temperature that the fully lithiated phase of silicon is actually $Li_{15}Si_4$ corresponding to a slightly lower capacity of 3579 mAh g^{-1} as opposed to the commonly used theoretical value of 4200 mAh g^{-1} based on $Li_{22}Si_5$.[65-67] At 0.1 C, the overall capacity of triple-layer asymmetric membrane is as high as 1100 mAh g^{-1} with an irreversible capacity loss (ICL) of 30.5% which is comparable to that of double-layer asymmetric membrane (Table 2). The ICL is slightly higher than that of single-layer asymmetric membrane (21.2%) because defective carbon may consume extra amount of lithium salts to form a stable SEI layer (Table 2).
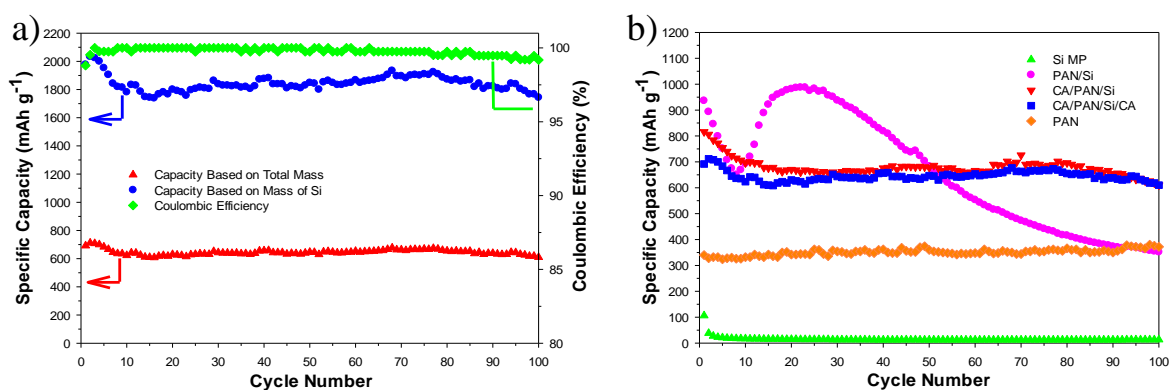
Figure 19: a) Cycling performance and coulombic efficiency of CA/PAN/Si/CA membrane; b) combined cycling performance of all batteries assembled with capacity based on overall mass.

Table 2: Irreversible capacity loss (ICL) of carbonized single-layer, double-layer and triple-layer asymmetric membranes.

Type of membrane	ICL (%)
CA/PAN/Si/CA; Triple Layer Asymmetric Membrane	30.5
CA/PAN/Si; Double Layer Asymmetric Membrane	34.4
PAN/Si; Single Layer Asymmetric Membrane	21.2
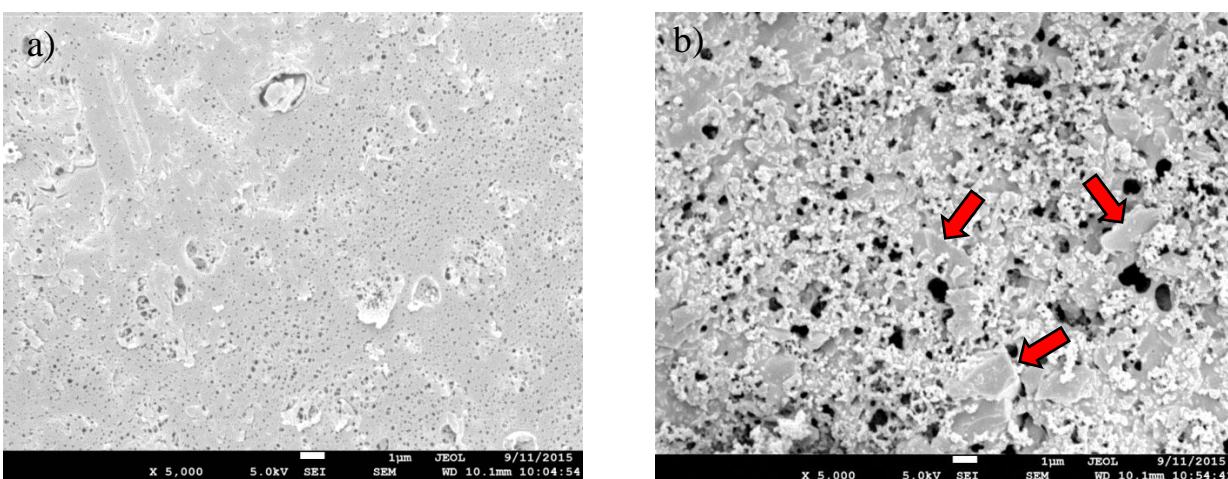
Figure 20: Scanning electron microscope images of a) as-prepared and b) carbonized single-layer asymmetric membrane containing Si MPs (PAN/Si, top-view). Note: arrows show Si micron powders

The differential capacity plot of triple-layer asymmetric membrane is shown in Figure 21a. During the first formation cycle with a current density of 100 mA g^{-1} (~0.05C), there is a sharp cathodic peak at 0.05 V, which can be attributed to the lithiation of crystalline Si MPs.[20] A sharp anodic peak at 0.46 V can be assigned to the de-lithiation of crystalline Li$_x$Si alloys.[20, 28, 68] After the first cycle, these two peaks become broader due to the amorphorization of Si and Li$_x$Si alloys.[61, 69] The corresponding voltage profiles are highly consistent with these differential capacity data (Figure 21c) The voltage profile of CA/PAN/Si/CA shows a long plateau around 0.05 V during

lithiation and another long plateau can be seen at ~0.46V while being de-lithiated (Figure 21c). During cycling, these plateaus become much less pronounced due to the Si becoming amorphous after the first formation cycle (Figure 21b). This is in good agreement with the differential plot after the first formation cycle. The capacity is decreased only ~40% when the C-rate is increased from 0.05 to 0.5 C (Figure 21d). This satisfactory rate performance can be attributed to the conductive porous carbon asymmetric structure with sufficient free volume to allow for rapid lithium ion diffusion. Furthermore, extra carbon coatings can also increase the electrical conductivity, thus making the interfacial electron transfer more efficient. Nyquist plots of the triple-layer asymmetric membrane electrode at the first and one hundredth cycles are shown in Figure 22. The plots were simulated using an equivalent circuit consisting of contact resistance (R_s), electrode double layer capacitance (C_{dl}), electrode charge transfer resistance (R_{ct}), SEI resistance (R_{SEI}) and SEI capacitance (C_{REI}), and Warburg diffusion impedance (W_d).[19] Simulated results (Table 3) show no significant change in R_{SEI} over the course of 100 cycles, suggesting the SEI layer is highly stable. In comparison, C_{dl} has been dramatically increased, whereas R_{ct} is reduced (Table 3). The drastic increase in C_{dl} can be related to the pulverization of bulky Si MPs into smaller Si NPs. Since NPs have a much higher surface area, C_{dl} is increased by more than two orders of magnitude after repeating lithiation/de-lithiation. Similarly, lithium ion diffusion length can be significantly shortened when Si MPs have been cracked into Si NPs after repeating lithiation/de-lithiation, thus decreasing R_{ct}. It is notable that even though the Si MP particles are fractured, they are still able to be charged because they are trapped in the conductive carbonaceous macro-channels in the asymmetric membranes.
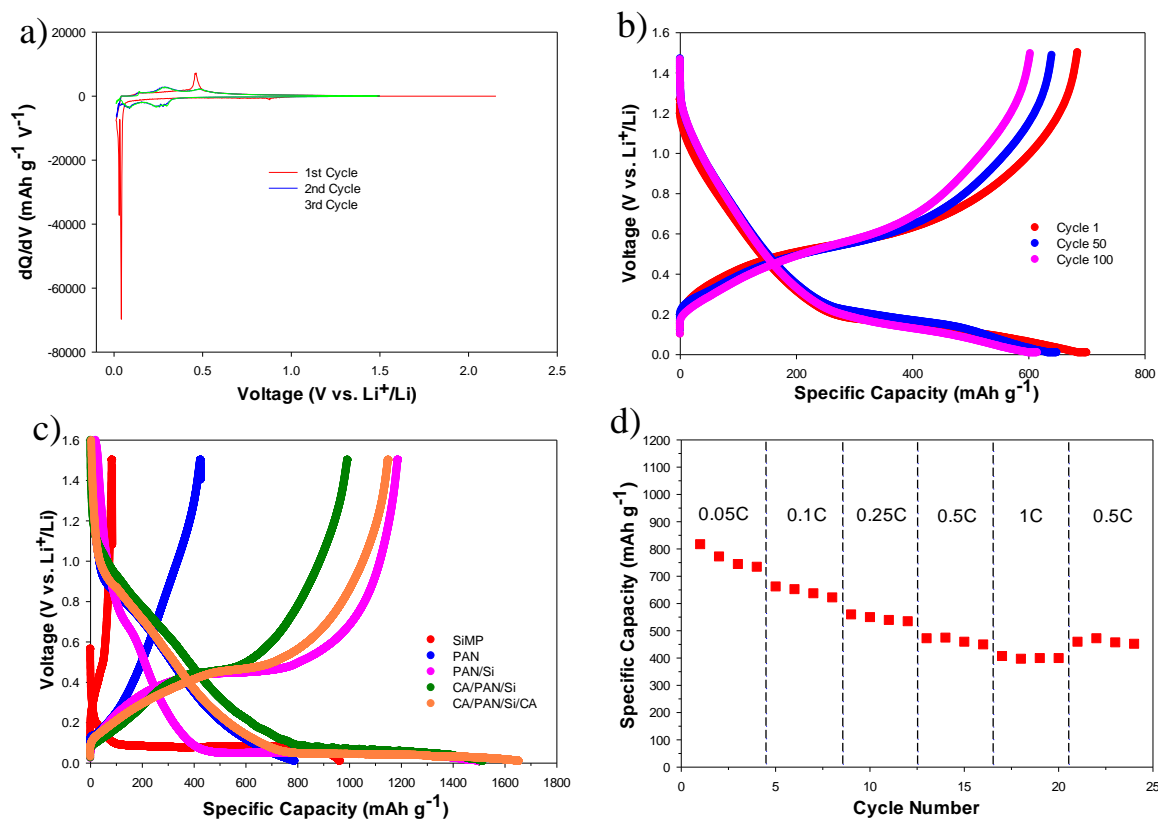
Figure 21: a) Differential voltage plot of the first 3 formation cycles of CA/PAN/Si/CA membrane electrode; b) Voltage profiles of CA/PAN/Si/CA membrane electrode at different cycles; c) Voltage profiles of the 1st formation cycle of all batteries assembled; and d) C-rate performance of CA/PAN/Si/CA membrane electrode.
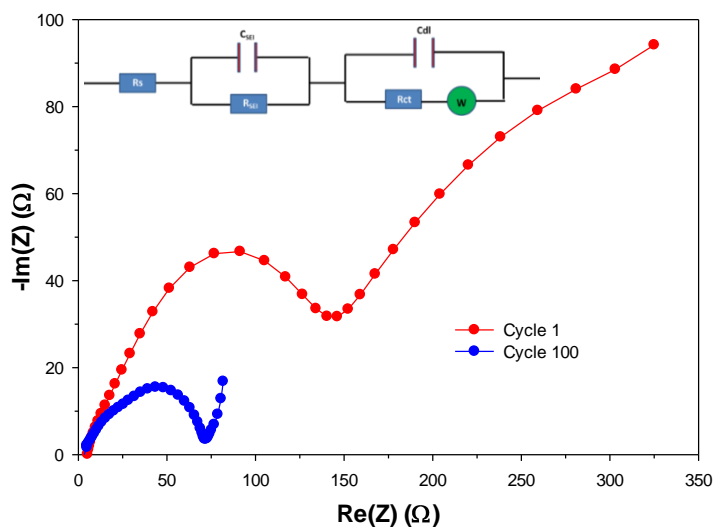
Figure 22: EIS Nyquist plots of CA/PAN/Si/CA triple-layer asymmetric membrane electrode at cycle 1 and cycle 100. The equivalent circuit used to calculate various parameters is also shown.

Table 3: Simulated results of Nyquist plots using an equivalent circuit as shown in Figure 12.

	Rs (Ω)	R$_{SEI}$ (Ω)	C$_{SEI}$ (F)	Rct (Ω)	Cdl (F)	Wd (Ω)
1st cycle	0.600	94.62	4.21×10^{-3}	149.5	1.04×10^{-4}	500.3
100th cycle	2.888	72.95	2.28×10^{-4}	34.83	7.46×10^{-2}	267.1

2.4.   Conclusion

It has been demonstrated that single-layer, double-layer, and triple-layer asymmetric membranes containing Si MPs can be fabricated using a straightforward phase inversion method with a much improved cycle life as LIB anode. The networking porous structure formed via a self-assembly method is beneficial to accommodating the large volume expansion of silicon-based anode. The carbonaceous coatings on the original single-layer PAN/Si asymmetric membranes can better prevent the loss of Si particles on the top surface after being pulverized, thus leading to a further increased cycle life (88% after 100 cycles). Such an outstanding cycle life has rarely been reported in literature for Si MPs-based anodes. This simplistic and scalable method may provide some inspiration for other researchers who are exploring the possibility of commercializing Si MPs-based anodes for LIB.

CHAPTER 3: Reinvigorating Reverse Osmosis Membrane Technology to Stabilize V_2O_5

Lithium Ion Battery Cathode

3.1.   Introduction

As previously mentioned in the introduction, current LIB cathodes are significantly lower in capacity than the anode materials. With extensive research being done on incorporating even higher capacity anode materials into LIBs, it becomes more and more important for cathode capacity to be improved. The most commonly used cathode material is $LiCoO_2$. Unfortunately, it suffers from a low capacity of only 140 mAh g^{-1}.[70] Not only does $LiCoO_2$ suffer from a low capacity, it is also expensive to manufacture and is not naturally as abundant as other potential replacements. V_2O_5 shows promise as a potential replacement for current commercial cathodes because of its relatively high capacity of 294 mAh g^{-1} when two lithium ions are inserted into one V_2O_5 unit.[42-43] Although V_2O_5 has a high capacity, its cycling performance is unsatisfactory due to a low electronic conductivity, ion diffusivity, and structural instabilities. In order to be used in LIBs, these issues need to be overcome. There have been many attempts to alleviate these issues utilizing nanostructurings such as: nanobelts, nanowires, and nanoparticles.[42-43, 71] These nanomaterials seek to eliminate the issues plaguing V_2O_5 by using materials small enough in diameter to improve the electrical conductivity and ionic diffusivity by shortening diffusion lengths for electrons and lithium ions to allow for efficient electron transfer and increased ionic diffusivity. Also, the addition of conductive additives such as graphene (GH) has been shown to further increase the conductivity.

Asymmetric membranes are an ideal candidate to alleviate the volume expansion issues as demonstrated in Chapter 2. This same method will be employed along with sol-gel chemistry to produce nano-sized V_2O_5 particles embedded within the asymmetric structure. These membranes

will undergo a series of heat treatments to make them electrically conductive. By adding GH into these membranes, the rate performance can be even greater than membranes with traditional carbon black additives.

3.2.   Experimental

3.2.1.   Synthesis of V_2O_5 asymmetric membranes using a phase inversion method combined with sol-gel chemistry

First, 0.5 g of polysulfone ($M_n \approx$ 60,000, pellets, Acros) was dissolved in 5 mL N-methyl-2-pyrrolidone (NMP) (Sigma Aldrich, >99.5%) under sonication (Bransonic CPX3800H) followed by adding 0.1 g carbon black (CB, TIMCAL SUPER C45 with a surface area of 45 m^2 g^{-1}) or 0.1 g graphene (GH, cheaptubes.com, >98 wt.%, 20-100 nm in diameter, >750 m^2/g) into the polymeric solution. Then 2.0 g of vanadium (V) oxytriethoxide (VOTEO, 95%, Acros Organics) was mixed with the polymeric solution containing CB or GH by 15 min vortexing and 5 min sonication. The mixture was coated onto a glass plate using a doctor blade with set to deliver a wet thickness of ~150 µm. The coated glass plate was immediately immersed into deionized water (~18 MΩ) for phase inversion. The as-formed asymmetric membrane separated from the glass substrate naturally after ~5 minutes. Finally, the asymmetric membrane was dried and treated at high temperatures using a Lindberg/Blue M™ 1100°C tube furnace with a ramp rate of ~60°C min^{-1}. The membranes were treated at high temperatures via a two-step method: 1) the membranes were first carbonized at 500°C for 1 hour under the protection of high purity helium gas (99.9999%, Airgas He UHP300) of 200 sccm flow rate to facilitate electrical conductivity while maintaining the porous structure and 2) the membranes were then heated in air from room temperature to 400°C in 5 minutes or heated in air at 300°C for 1.5 hrs to retrieve vanadium (V) oxide. The asymmetric membrane prepared using CB and annealed at 400°C in air in 5 minutes

was labeled V_2O_5 EO-400 CB; the asymmetric membrane prepared using CB and heated at 300°C in air for 1.5 hours was labeled as V_2O_5 EO-300 CB; and the asymmetric membrane prepared using graphene and heated at 300°C in air for 1.5 hours was labeled V_2O_5 EO-300 GH.

3.2.2. *Characterization of V_2O_5 asymmetric membranes*

A Field Emission Scanning Electron Microscopy (JEOL JSM-7600F) attached with Transmission Electron Detector (TED) was employed for membrane morphological and structural characterization. High Resolution Transmission Electron Microscopy (HRTEM) characterization was performed using a JEM 2100F TEM (JEOL Ltd., Japan) operated at accelerating voltages of 120 to 200 kV. A ThermoScientific DXR SmartRaman Spectrometer was operated using a 532 nm laser of 5 mW, an objective lens of 10X, and a total integration time of 120 seconds. Powder X-ray diffraction (Scintag XGEN-4000) was taken using a Cu K_α radiation ($\lambda = 0.1542$ nm) from 10 to 70° (2Θ) with a step rate of 0.1° per second. The acceleration voltage and current are 40 kV and 15 mA, respectively. V_2O_5 asymmetric membranes were also analyzed for their elemental composition and oxidation states using an X-ray photoelectron spectroscopy (PHI 5000 Versaprobe XPS system from Physical Electronics, Inc.), which employed monochromatic Al K_α X-rays of energy 1486.6 eV. Powder samples were mounted onto the XPS sample holder using a double-sided carbon tape. An X-ray spot size of 200 mm at ~ 50 W was used for data acquisition. Survey scans at pass energy of 117 eV were performed for the chemical elemental identification. To determine the chemical bonding states, we acquired region spectra at pass energy of 23.5 eV. The takeoff angle was kept constant at 45°. The specific surface areas of four kinds of asymmetric membranes were measured using a Micromeritics ASAP 2020 Surface Area and Porosity Analyzer, which were calculated using Brunauer-Emmett-Teller (BET) method. Membrane samples were degassed at 50 μTorr and 300°C for 30 minutes. The content of V_2O_5 was determined

by a thermogravimetric analyzer (TA Instruments G50 TGA) using compressed air as the purging gas (Ultra Zero, Airgas). The flow rate of the compressed air gas is 20 mL min^{-1} and the temperature was ramped from 25 to 550°C at a rate of 10°C min^{-1}, and then held at 550°C for 15 minutes. Pure V_2O_5 micron-size particles (10 meshes, 99.6% min., Alfa Aesar) were used as a reference in Raman, PXRD, XPS and TGA analysis.

3.2.3. *Electrochemical evaluation of asymmetric membranes as LIB Cathodes*

V_2O_5 electrodes were prepared by adhering the asymmetric membranes directly onto aluminum discs (15 mm in diameter and 18 µm thick from MTI Corporation) using a glue consisting of 0.1 g carbon black and 0.1 g polyvinylidene fluoride (PVDF, MTI Corporation) dispersed in 3 mL NMP. The uncalendered electrode was dried at 120 ^{0}C for at least 4 hrs to remove residual NMP and H_2O moisture. The final mass of membrane materials per electrode is ~2 mg. The electrode was then assembled into 2032-type coin cells using lithium metal (EQ-Lib-LiC25, MTI Corporation) as the counter electrode and 60 µL 1 M $LiPF_6$ dissolved in ethylene carbonate (EC), dimethyl carbonate (DMC) and diethyl carbonate (DEC) with a volume ratio of 1:1:1 (MTI Corporation) as the electrolyte. Inside the glove box (LCPW, LC Technology Solutions, INC.), oxygen and water concentrations were maintained below 1 ppm. The membrane separator is ethylene/polypropylene blend with pore sizes 20-30 nm (MTI Corporation). Galvanostatic cycling tests of LIB half-cells were conducted using a multi-channel Potentiostat/EIS (BIO-LOGIC VMP3) at room temperature. The voltage window is 2.00-3.60 V (vs. Li/Li$^+$). For both rate performance and cyclability tests, the cells were charged and discharged with the same current density. The cells were subject to five formation cycles at 20 mA g^{-1} before any subsequent tests. Charging rates of 0.1, 0.2, 0.5 and 0.1C were applied to test the cell rate performance. Long term cyclability tests were performed at 0.5C. During the cyclic voltammetry

measurements, the voltage was scanned from 2.00 to 3.60 V at a rate of 0.05 mV s^{-1}. Electrochemical impedance spectroscopy (EIS) measurements were carried out in the frequency range of 0.1 Hz–1 MHz with AC amplitude of 10 mV.

3.3. Results and Discussion

3.3.1. Fabrication of V_2O_5 asymmetric membranes

V_2O_5 asymmetric membranes were prepared using an adapted phase inversion method that has been utilized to fabricate polymeric asymmetric membranes on a large scale for water desalination and purification.[58, 72] In the phase inversion process, the thin film consisting of NMP, PS, VOTEO and CB (or GH) was immersed into water (non-solvent) to generate two phases, polymer rich and polymer lean phases, resulting in the spontaneous formation of asymmetric porous structure. The purpose of adding the CB or GH is to not only increase electrical conductivity, but also to serve as a scaffolding to prevent the asymmetric structure from collapsing upon carbonization. The as-formed inorganic/polymeric membranes were then carbonized to make the membrane conductive. The carbonized membranes were annealed in air at various temperatures to obtain V_2O_5 asymmetric membranes. The extra annealing step is necessary due to the reduction of V_2O_5 into other charge states upon carbonization. It is notable that the membrane annealed at higher temperature in air is more fragile than the one annealed at lower temperature, because more carbon material is lost during the higher temperature annealing. We have shown this method is highly scalable as evident by a piece of 6 in × 2 in membrane shown in Figure 23a. Cross-sectional SEM images confirm the membrane possesses the asymmetric structure with a layer of nanopores on its top surface and macropores underneath the nanopores (Figure 23b).
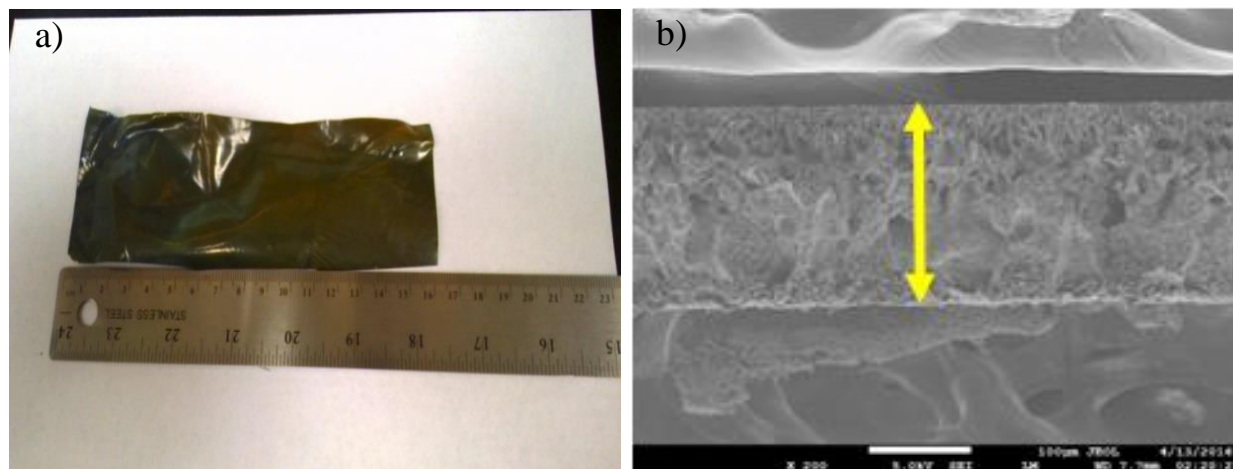
Figure 23: a) Photo of V_2O_5 asymmetric membrane prior to carbonization; b) cross-sectional SEM image of the uncarbonized V_2O_5 asymmetric membrane.

3.3.2. *Characterization of V_2O_5 asymmetric membranes*

SEM images of V_2O_5 asymmetric membranes after being annealed in air clearly show that the top layer is nanoporous, whereas the bottom layer is macroporous. The thickness of V_2O_5 EO-300 CB asymmetric membrane is about 140 (Figure 24d). At a higher temperature of 400°C with an annealing time of only 5 minutes, the thickness is reduced to 120 µm (Figure 24b). The reduced thickness is ascribed to higher shrinkage induced by more carbon removal at higher oxidation temperature, which is also confirmed by our TGA analysis. In comparison, the V_2O_5 EO-300 GH membrane shown in Figure 24f is much thinner than other two types of membranes (~70 µm). It may be due to the strong π-π interactions between graphene sheets, leading to a denser packing. The SEM image in Figure 25 confirms that the reference sample consists of micron size particles. As revealed by the HRTEM images in Figure 26, a d-spacing of 0.34 nm was observed within both V_2O_5 EO-300 CB and V_2O_5 EO-300 GH, which is corresponds to the (110) lattice plane in orthorhombic V_2O_5.[52] The morphologies of V_2O_5 nanoparticles in V_2O_5 EO-300 CB and V_2O_5 EO-300 GH are quite different. Spherical particles are observed in V_2O_5 EO-300 CB and platelet-like

particles can be seen in V_2O_5 EO-300 GH. It is likely that the morphology of the additives (spherical CB and platelet-like GH) can affect the shapes of V_2O_5 nanoparticles when using a sol-gel chemistry method.
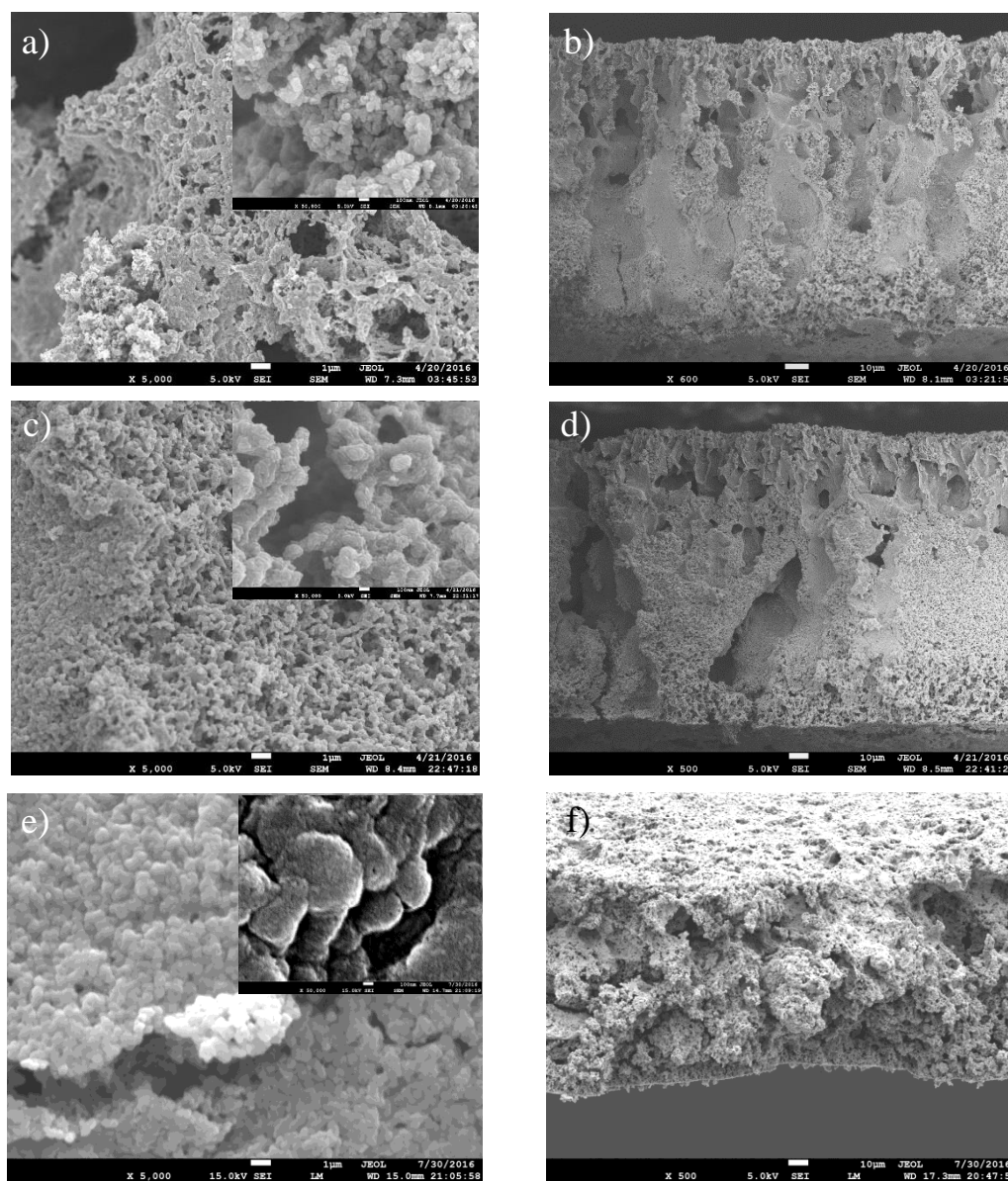
Figure 24: SEM images of V_2O_5 EO-400 membrane a) surface-view and b) cross-sectional view of; V_2O_5 EO-300 CB membrane c) top-view and d) cross-sectional view; and V_2O_5 EO-300 GH membrane e) top-view and f) cross-sectional view.
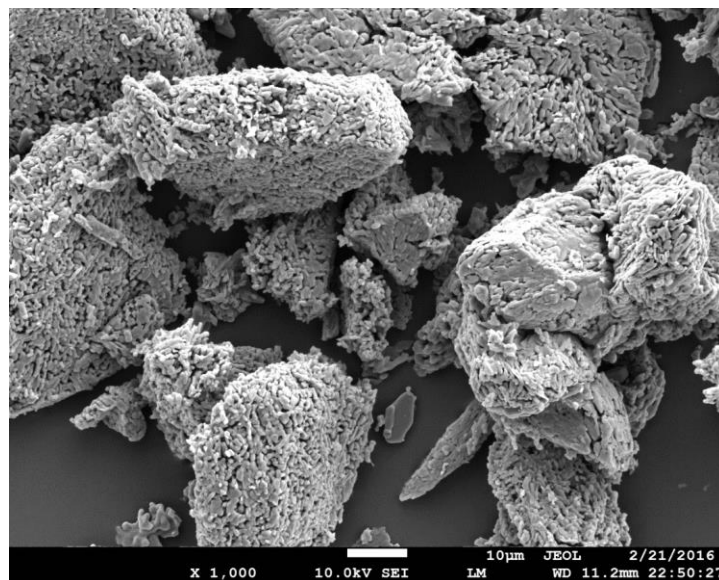
Figure 25: SEM image of V_2O_5 micron-particles used as a reference for PXRD, XPS, Raman, and TGA.
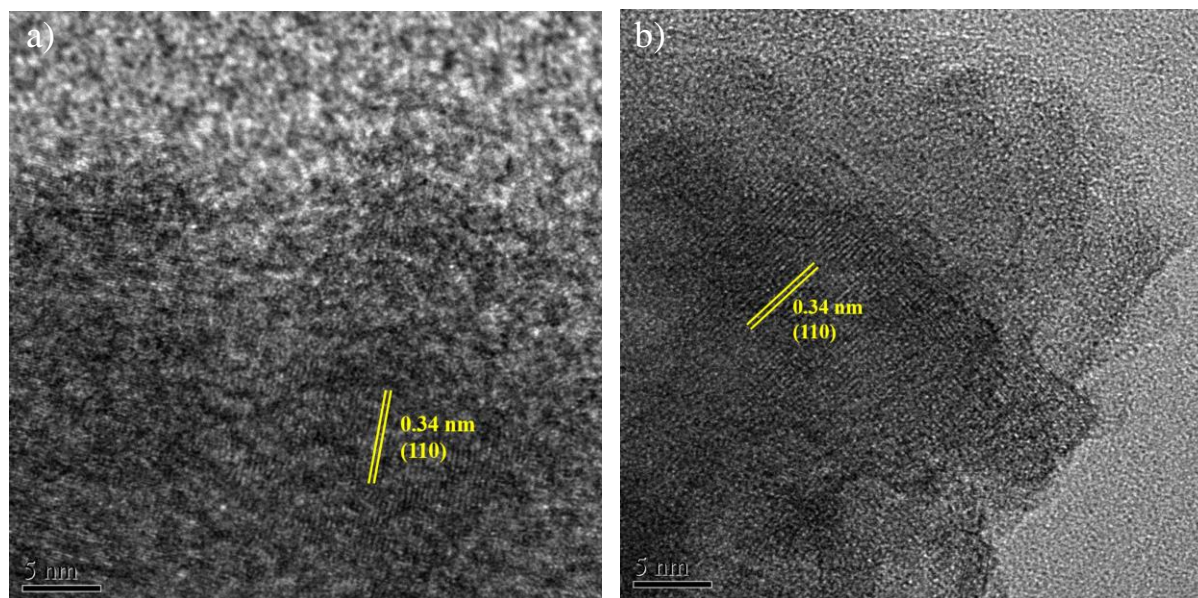
Figure 26: High-Resolution TEM images of a) V_2O_5 EO-300 CB and b) V_2O_5 EO-300 GH membranes. Scale bars are 5 nm.

Raman spectra of V_2O_5 EO-400 CB, EO-300 CB and EO-300 GH are fully consistent with the pure orthorhombic V_2O_5 reference (Figure 27a).[73] G and D Raman peaks from graphitic materials can't be seen because the content of carbon is low and the background scattering is very

strong due to the highly porous structure. Powder X-ray diffraction data further confirm the formation of crystalline orthorhombic V_2O_5 (JCPDS 41-1426) in all types of asymmetric membranes annealed in air (Figure 27b). The peaks of V_2O_5 asymmetric membranes are much broader than those of micron-size V_2O_5 reference, indicating the presence of nanoscale V_2O_5 particles. The sharp peak at 27° from V_2O_5 EO-300 GH sample is characteristic of graphitic materials.[74] It is notable that V_2O_5 EO-300 CB sample also has a peak centered around ~27°, which may be due to the presence of trace amount of V_xO_2 or graphitic materials.[71] This peak didn't show up for V_2O_5 EO-400 CB where carbon content is much lower.
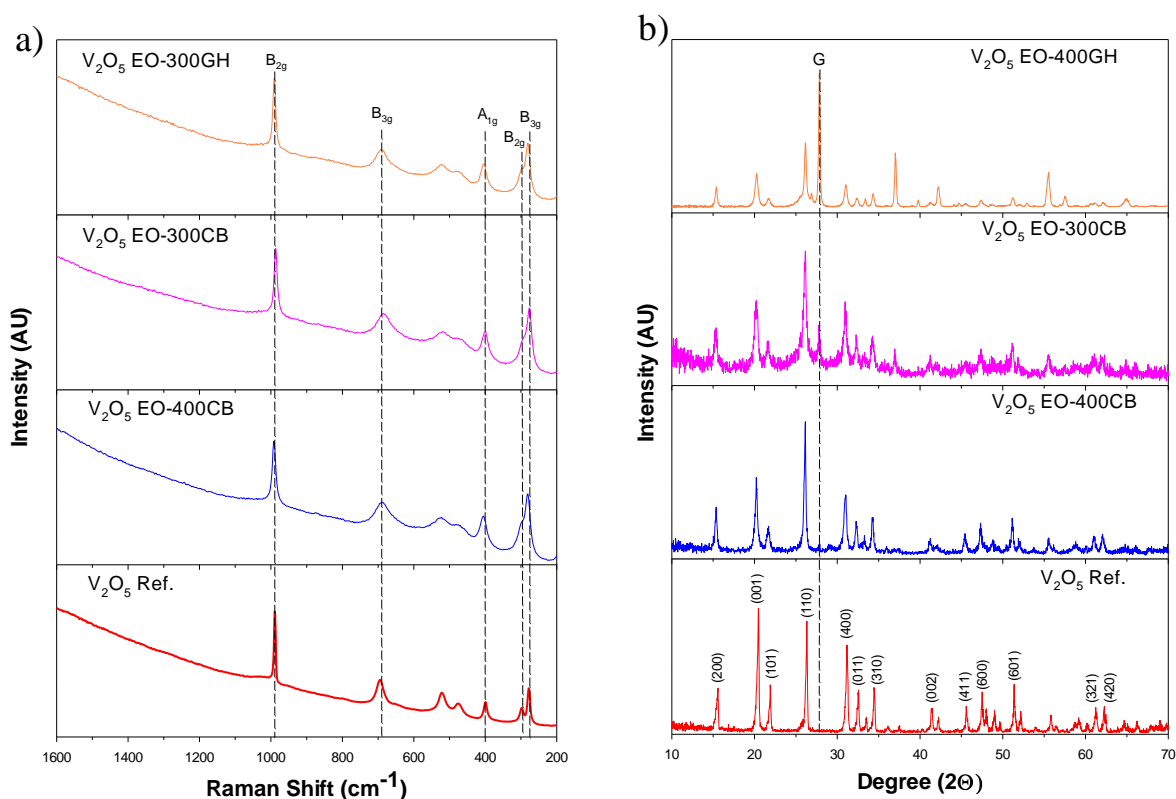
Figure 27: a) Raman spectra of all carbonized membranes and reference; b) Powder X-Ray Diffraction of all carbonized membanes and reference.

The XPS spectra of V 2p and O 1s are shown in Figure 28. The peaks centered at 517.2 and 524.7 eV are ascribed to V^{5+} $2p_{3/2}$ and V^{5+} $2p_{1/2}$, respectively, while O 1s peak is around 530.1 eV.[75] The XPS data supports that there are no vanadium in other oxidation states.
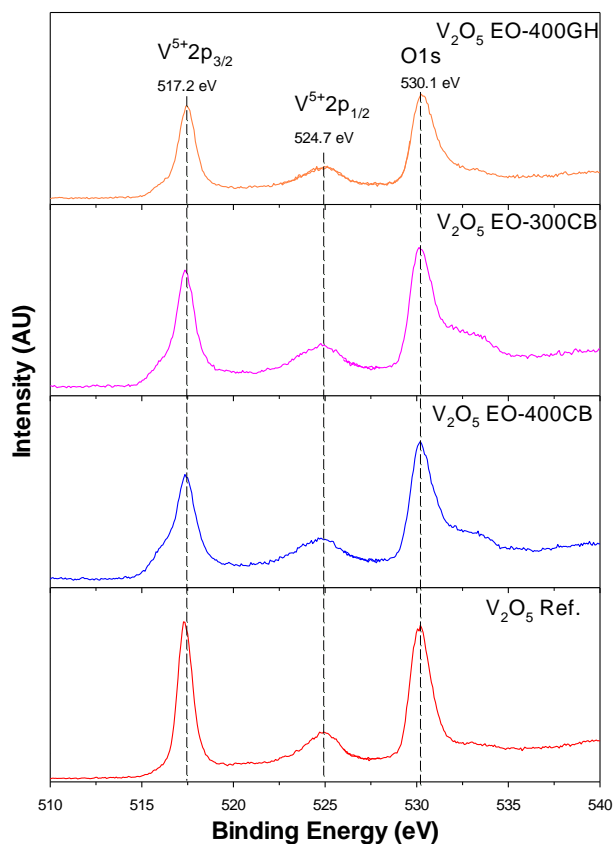
Figure 28: X-ray photoelectron spectroscopy spectra of various V_2O_5 asymmetric membranes. Note: standard V_2O_5 spectrum is collected for reference.

The content of V_2O_5 in the carbonized membranes was determined using thermogravimetric (TGA) analysis (Figure 29). The mass percentages of V_2O_5 were calculated to be 94.54, 91.44 and 74.7 wt. % in V_2O_5 EO-400 CB, V_2O_5 EO-300 CB and V_2O_5 EO-300 GH, respectively. The lower content of carbon in V_2O_5 EO-400 CB is due to the rapid oxidation of carbon at 400°C than 300°C in air. The content of carbon in V_2O_5 EO-300 GH is much higher than

other two types of membranes because it requires higher temperature to oxidize crystalline graphene.[76]
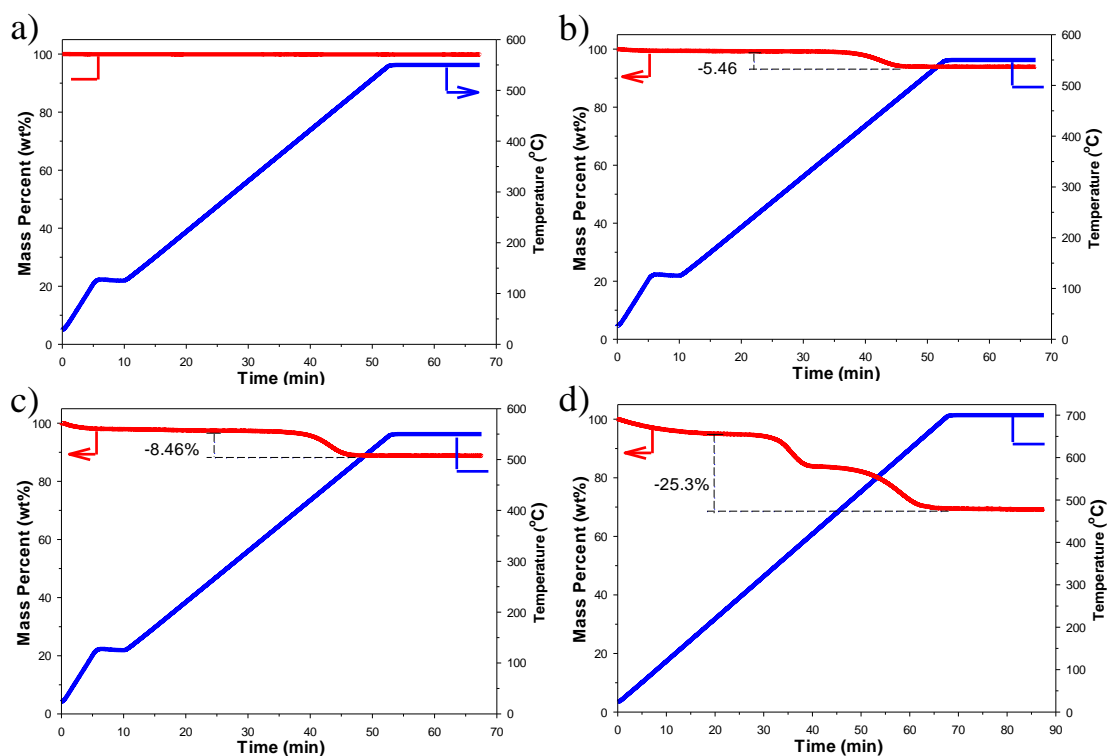
Figure 29: Thermogravimetric analysis of various V_2O_5 asymmetric membranes using compressed air as the purging gas a) V_2O_5 reference, b) V_2O_5 EO-300 CB, c) V_2O_5 EO-400 CB and d) V_2O_5 EO-300 GH.

The specific surface area was calculated by the Brunauer Emmett and Teller (BET) method (Table 4). The specific surface areas of V_2O_5 EO-400 CB, V_2O_5 EO-300 CB and V_2O_5 EO-300 GH were found to be 42.5, 21.7 and 20.5 m^2 g^{-1}, respectively. The higher specific area of V_2O_5 EO-400 CB is possibly caused by the greater loss of carbon during annealing which may create more nanopores.

Table 4: BET surface area of various V_2O_5 membranes.

Type of membrane	BET specific Area (m^2/g)
V_2O_5 EO-400 CB	42.5
V_2O_5 EO-300 CB	21.7
V_2O_5 EO-300 GH	20.5

*3.3.3. Electrochemical properties of V_2O_5 asymmetric membranes as LIB cathodes*

Electrochemical performance of V_2O_5 cathodes is shown in Figure 30a. All three cathodes fabricated with asymmetric membranes demonstrate excellent rate performance, which can be attributed to the high surface area, nanoporous structure and conductive carbon coating on V_2O_5 nanoparticles. These cathodes delivered a capacity close or above 200 mAh g^{-1} at 0.1C, which is much higher than conventional cathode materials (Figure 30b).[77] V_2O_5 EO-400 CB has the highest initial capacity of 174 mAh g^{-1} at 0.5C mainly due to its high surface area (Figure 30a).[78] However, it experiences a 7% decrease after 120 cycles which is the greatest of the three membranes. Such a cyclability is still excellent in comparison with traditional cathode materials. In comparison, V_2O_5 EO-300 CB cathode demonstrates an initial capacity of 159 mAh g^{-1} at 0.5C, which increases slightly by ~8% in the first 150 cycles and then degrades gradually to 133 mAh g^{-1} after 380 cycles for an overall retention of 84% from the first cycle. The V_2O_5 EO-300 GH cathode demonstrates the most outstanding cycling performance. The capacity actually gradually increases by ~8% throughout 380 cycles, indicating that V_2O_5 can be more efficiently lithiated during the cycling process. The initial capacity increase in the V_2O_5 EO-300 CB and V_2O_5 EO-300 GH may be attributed to the volume expansion in the electrodes. The expansion may open up some closed pores and enable more V_2O_5 to be accessible for lithiation and delithiation. The continuous capacity increase and outstanding stability in V_2O_5 EO-300 GH implies the existence of grapheme

renders excellent structural and mechanical stability over CB where capacity started decreasing after 150 cycles in V_2O_5 EO-300 CB cathodes.
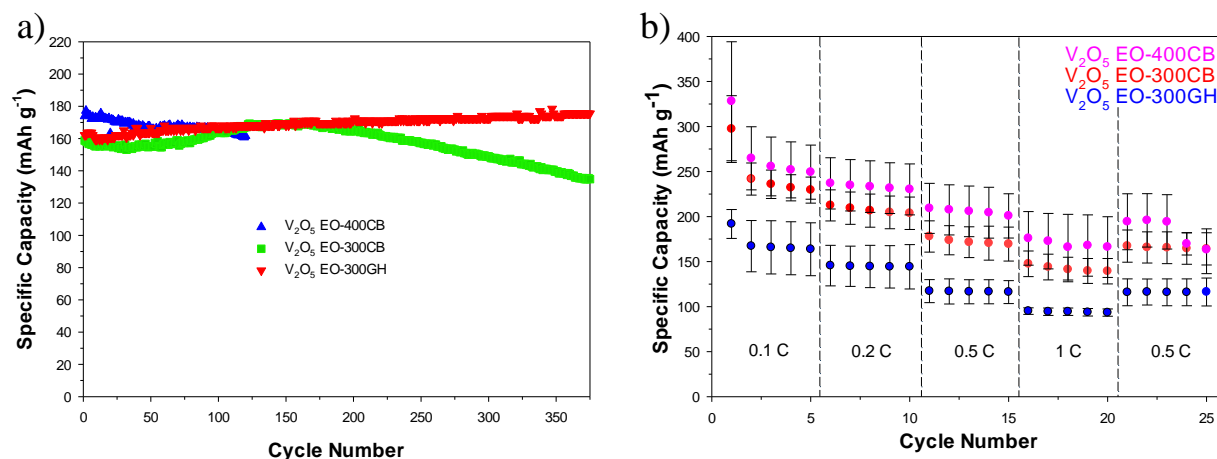
Figure 30: a) cycling performance of V_2O_5 cathodes and b) C-rate performance of V_2O_5 cathodes with standard error bars.

Figure 31a and 31b show normalized voltage profiles. The gap between the charge and discharge plateaus at half normalized capacity represents the polarization. The polarization in the V_2O_5 EO-300 GH cathodes is lower than V_2O_5 EO-300 CB cathode in the first cycle. This corresponds with a smaller overpotential. For example, the polarization at 0.5 normalized capacity is 0.36 V and 0.29 V for V_2O_5 EO-300 CB and V_2O_5 EO-300 GH, respectively. The polarization further reduces to 0.24 V after 380 cycles for V_2O_5 EO-300 GH at 0.5 normalized capacity. This reduction in polarization may suggest that over time the conductivity and/or ionic diffusivity improves over the course of cycling. This hypothesis may help to explain the capacity increase over the course of cycling which was believed to be caused by the volume expansion allowing more efficient lithium storage. In contrast, the polarity increases slightly up to 0.48 V for V_2O_5 EO-300 CB after 380 cycles. The polarization changes in V_2O_5 EO-300 GH and V_2O_5 EO-300 CB cathodes explain the difference in their cyclability behaviors in Figure 30a.
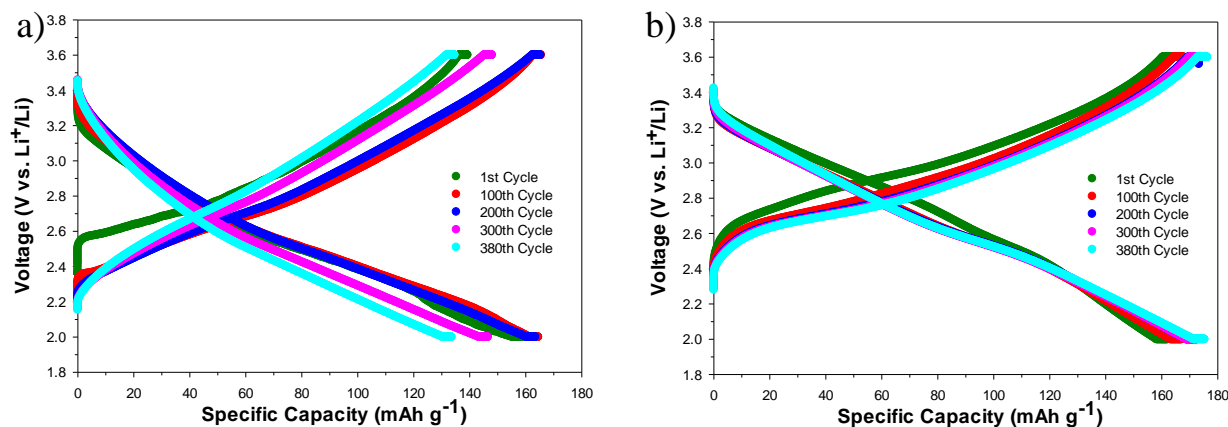
Figure 31: Voltage profiles during cycling of: a) V_2O_5 EO-300 CB and b) V_2O_5 EO-300 GH.

The cyclic voltammetry (CV) of V_2O_5 EO-300 CB and V_2O_5 EO-300 GH membrane electrodes are shown in Figure 32. For V_2O_5 EO-300 CB electrode, three lithiation peaks centered at 3.36, 3.16 and 2.23 V are ascribed to the phase transitions of ($\alpha \leftrightarrow \varepsilon$), ($\varepsilon \leftrightarrow \delta$), and ($\delta \leftrightarrow \gamma$) respectively.[48] The corresponding electrochemical reactions are explained in detail in section 1.6. The 2.23 V lithiation peak is positively shifted during CV cycling especially for V_2O_5 EO-300 CB, indicating an increasing conductivity which is consistent with the reduced impedance as shown in Figure 33a. This fact is also consistent with the voltage profiles shown in Figure 31, where the polarization reduces after cycles. Three delithiation peaks around 2.60, 3.26 and 3.46 V are assigned to ($\gamma \leftrightarrow \delta$), ($\delta \leftrightarrow \varepsilon$), and ($\varepsilon \leftrightarrow \alpha$) phase transitions, respectively. Additionally, the large voltage difference between lithiation and delithiation reactions implies that it is quite resistive for lithium ions to diffuse out of $Li_2V_2O_5$.
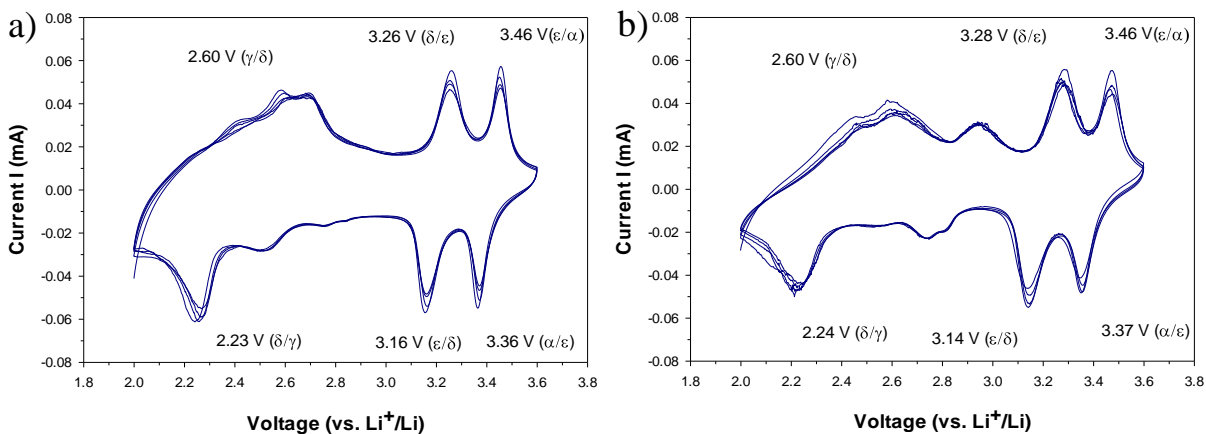
Figure 32: Cyclic voltammetry of a) V_2O_5 EO-300 CB and b) V_2O_5 EO-300 GH

EIS spectra of V_2O_5 EO-300 CB and V_2O_5 EO-300 GH cathodes are shown in Figure 33. It can be clearly seen that the charge transfer resistance was significantly changed for V_2O_5 EO-300 CB after the cycling test, implying that there was a dramatic electrode evolution during the cycling. In addition, the ohmic resistance increased after cycles for V_2O_5 EO-300 CB, probably due to the partial electrode detachment from the current collector after repeated cycles. This is in close agreement with the voltage profile data. In comparison, the EIS spectra of V_2O_5 EO-300 GH are very similar to each other before and after the cycling test. This fact supports that the electrode is integral and SEI layer is highly stable during the repeated lithiation/delithiation.
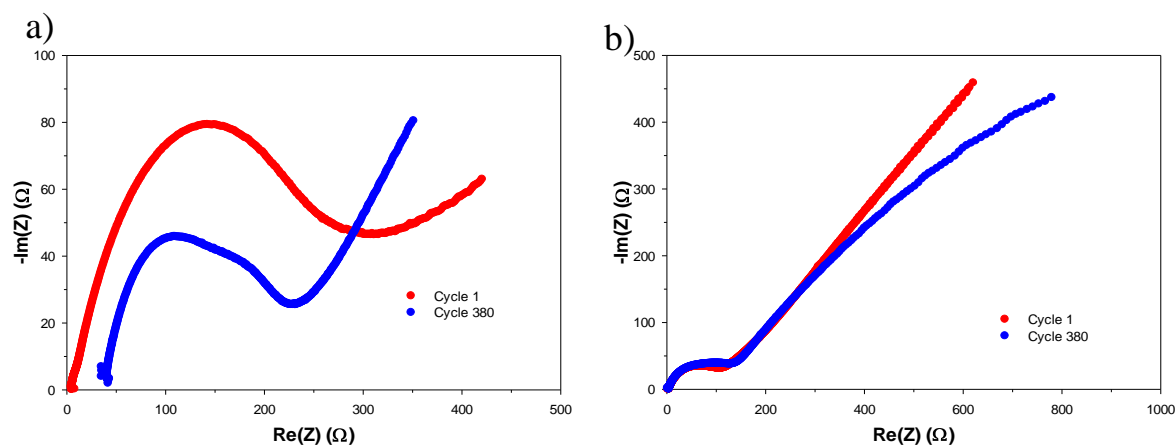
Figure 33: EIS Nyquist Plots of: a) V_2O_5 EO-300 CB and b) V_2O_5 EO-300 GH.

3.4.   Conclusion

Three types of V_2O_5 asymmetric membranes are fabricated using an adapted phase inversion method combined with sol-gel chemistry. The three-dimensional nanoporous structure and carbon coating can dramatically improve the electrochemical performance of V_2O_5-based cathodes. The annealing temperature and choice of conductive additives also have a significant impact on the cycling performance. High-temperature annealing can shorten the cycling life due to the large loss of conductive additives at elevated temperatures. The addition of GH benefits electrode stability and also affects the morphology of V_2O_5 nanoparticles. The nearly 100% capacity retention after 380 cycles, straightforward fabrication process and excellent rate performance make this method outstanding from other approaches in literature.

CHAPTER 4: Concluding Remarks and Future Outlook

It is demonstrated that the utilization of asymmetric membranes is an effective method to stabilize the structures of high capacity anode and cathode materials. They possess a unique structural advantage over other literature methods to tame volume expansion and unstable interphase issues. Also, these membranes are easily fabricated using a facile phase inversion method and can be produced on a large scale using commercial roll-to-roll membrane technology. Not only is the process simple and scalable, it is also relatively safe as it does not require dangerous chemicals to fabricate them as many other methods require. This method proves that the addition of inorganic solid materials into the polymeric solution does not throw off the phase diagram and allows for the particles to be embedded within. Likewise, the addition of an organic precursor dissolved in the solvent does not affect the phase diagram either. These additions to asymmetric membranes have never been reported in the literature by any other groups. This makes this method ideal for a wide range of other materials besides the ones studied in this thesis.

However, this method is currently unfit for large scale commercialization as the carbonization step causes the membranes to become very brittle and difficult to handle without breaking. To improve on this work in the future, the carbonization step should be avoided if possible. Currently the carbonization step is necessary because before carbonization the membranes are not electrically conductive and thus are unsuitable for being used in a LIB. There are a few possible strategies that may help circumvent the carbonization step. One suggested approach is to increase the amount of conductive additives in the membrane to the point where it becomes conductive enough to be used in a battery. However, the conductivity will likely be lower than conventional batteries further limiting their performance at a fast charging rate. Another idea is to fabricate the active materials into one-dimensional nanowires and add highly conductive

carbon nanotubes to the solution as well. Ideally, the nanowires and carbon nanotubes would become intertwined with each other providing enough contact points for electrons to be efficiently shuttled and thus allowing the conductivity to be high enough for use in LIBs.

REFERENCES

1.   Ohzuku, T.; Brodd, R. J. An overview of positive-electrode materials for advanced lithium-ion batteries. *Journal of Power Sources* **2007,** *174* (2), 449-456.

2.   Tarascon, J. M.; Armand, M. Issues and challenges facing rechargeable lithium batteries. *Nature* **2001,** *414* (6861), 359.

3.   Byrd, I.; Wu, J. Asymmetric Membranes Containing Micron-Size Silicon for High Performance Lithium Ion Battery Anode. *Electrochimica Acta* **2016,** *213*, 46-54.

4.   Singh, R. *Lithium-Ion Battery Market by Material Type (Cathode, Anode, Electrolytic solution, Foils, Binders, Separators) and Industry Vertical (Smartphones, UPS, Cars, Aircraft, Busses, Trucks, Mining equipment, Smart Grid, Games, Gardening tools) - Global Opportunity Analysis and Industry Forecast, 2015-2022*; Electronic Systems and DevicesAllied Market Research: 2016.

5.   Zubi, G.; Dufo-López, R.; Pardo, N.; Pasaoglu, G. Concept development and techno-economic assessment for a solar home system using lithium-ion battery for developing regions to provide electricity for lighting and electronic devices. *Energy Conversion and Management* **2016,** *122*, 439-448.

6.   Gyuk, I.; Johnson, M.; Vetrano, J.; Lynn, K.; Parks, W.; Handa, R.; Kannberg, L.; Hearne, S.; Waldrip, K.; Braccio, R. *Grid Energy Storage*; Department of Energy: 2013.

7.   Wang, S.-C. S. In *Advanced Secondary Batteries And Their Applications for Hybrid and Electric Vehicles*, 2011 IEEE Green Energy Conferencee, Long Beach, CA, December 5, 2011; Long Beach, CA, 2011.

8.   Nexeon. About Li-ion batteries. https://www.nexeon.co.uk/about-li-ion-batteries/ (accessed January 4).

9.   Lee, H.; Yanilmaz, M.; Toprakci, O.; Fu, K.; Zhang, X. A review of recent developments in membrane separators for rechargeable lithium-ion batteries. *Energy & Environmental Science* **2014,** *7* (12), 3857-3886.

10.   McCormac, K. *Electrospun Titanium Dioxide and Silicon Composite Nanofibers for Advanced Lithium Ion Batteries*. Digital Commons@Georgia Southern.

11.   Smith, K.; Wang, C.-Y. Power and thermal characterization of a lithium-ion battery pack for hybrid-electric vehicles. *Journal of Power Sources* **2006,** *160* (1), 662-673.

12.   Winter, M.; Brodd, R. J. What Are Batteries, Fuel Cells, and Supercapacitors? *Chemical Reviews* **2004,** *104* (10), 4245-4270.

13.   Scrosati, B.; Garche, J. Lithium batteries: Status, prospects and future. *Journal of Power Sources* **2010,** *195* (9), 2419-2430.

14.   Balakrishnan, P. G.; Ramesh, R.; Prem Kumar, T. Safety mechanisms in lithium-ion batteries. *Journal of Power Sources* **2006,** *155* (2), 401-414.

15.   Wang, Q.; Ping, P.; Zhao, X.; Chu, G.; Sun, J.; Chen, C. Thermal runaway caused fire and explosion of lithium ion battery. *Journal of Power Sources* **2012,** *208*, 210-224.

16.   Wang, Q.; Ping, P.; Sun, J. Catastrophe analysis of cylindrical lithium ion battery. *Nonlinear Dynamics* **2010,** *61* (4), 763-772.

17.   Abada, S.; Marlair, G.; Lecocq, A.; Petit, M.; Sauvant-Moynot, V.; Huet, F. Safety focused modeling of lithium-ion batteries: A review. *Journal of Power Sources* **2016,** *306*, 178-192.

18.   Byrd, I.; Chen, H.; Webber, T.; Li, J.; Wu, J. Self-assembled asymmetric membrane containing micron-size germanium for high capacity lithium ion batteries. *RSC Advances* **2015,** *5* (113), 92878-92884.

19.   Li, B.; Yao, F.; Bae, J. J.; Chang, J.; Zamfir, M. R.; Le, D. T.; Pham, D. T.; Yue, H.; Lee, Y. H. Hollow carbon nanospheres/silicon/alumina core-shell film as an anode for lithium-ion batteries. *Scientific Reports* **2015,** *5*, 7659.

20.   Nitta, N.; Yushin, G. High-Capacity Anode Materials for Lithium-Ion Batteries: Choice of Elements and Structures for Active Particles. *Particle & Particle Systems Characterization* **2014,** *31* (3), 317-336.

21.   Cui, L.-F.; Yang, Y.; Hsu, C.-M.; Cui, Y. Carbon−Silicon Core−Shell Nanowires as High Capacity Electrode for Lithium Ion Batteries. *Nano Letters* **2009,** *9* (9), 3370-3374.

22.   Zheng, H.; Li, J.; Song, X.; Liu, G.; Battaglia, V. S. A comprehensive understanding of electrode thickness effects on the electrochemical performances of Li-ion battery cathodes. *Electrochimica Acta* **2012,** *71*, 258-265.

23.   Zhao, R.; Liu, J.; Gu, J. The effects of electrode thickness on the electrochemical and thermal characteristics of lithium ion battery. *Applied Energy* **2015,** *139*, 220-229.

24.   Tian, H.; Xin, F.; Wang, X.; He, W.; Han, W. High capacity group-IV elements (Si, Ge, Sn) based anodes for lithium-ion batteries. *Journal of Materiomics* **2015,** *1* (3), 153-169.

25.   Guo, Q.; Zheng, Z.; Gao, H.; Ma, J.; Qin, X. SnO_2/graphene composite as highly reversible anode materials for lithium ion batteries. *Journal of Power Sources* **2013,** *240*, 149-154.

26.   Wu, J.; Chen, H.; Byrd, I.; Lovelace, S.; Jin, C. Fabrication of SnO_2 Asymmetric Membranes for High Performance Lithium Battery Anode. *ACS Applied Materials & Interfaces* **2016,** *8* (22), 13946-13956.

27.   Chen, Z.; Wang, C.; Lopez, J.; Lu, Z.; Cui, Y.; Bao, Z. High-Areal-Capacity Silicon Electrodes with Low-Cost Silicon Particles Based on Spatial Control of Self-Healing Binder. *Advanced Energy Materials* **2015,** *5* (8), 1401826.

28.   Obrovac, M. N.; Krause, L. J. Reversible Cycling of Crystalline Silicon Powder. *Journal of The Electrochemical Society* **2007,** *154* (2), A103-A108.

29.   Wang, C.; Wu, H.; Chen, Z.; McDowell, M. T.; Cui, Y.; Bao, Z. Self-healing chemistry enables the stable operation of silicon microparticle anodes for high-energy lithium-ion batteries. *Nature Chemistry* **2013,** *5* (12), 1042-1048.

30.   Lee, S.-J.; Lee, J.-K.; Chung, S.-H.; Lee, H.-Y.; Lee, S.-M.; Baik, H.-K. Stress effect on cycle properties of the silicon thin-film anode. *Journal of Power Sources* **2001,** *97–98*, 191-193.

31.   Ruffo, R.; Hong, S. S.; Chan, C. K.; Huggins, R. A.; Cui, Y. Impedance Analysis of Silicon Nanowire Lithium Ion Battery Anodes. *The Journal of Physical Chemistry C* **2009,** *113* (26), 11390-11398.

32.   Yang, J.; Wang, Y.-X.; Chou, S.-L.; Zhang, R.; Xu, Y.; Fan, J.; Zhang, W.-x.; Kun Liu, H.; Zhao, D.; Xue Dou, S. Yolk-shell silicon-mesoporous carbon anode with compact solid electrolyte interphase film for superior lithium-ion batteries. *Nano Energy* **2015,** *18*, 133-142.

33.   McCormac, K.; Byrd, I.; Brannen, R.; Seymour, B.; Li, J.; Wu, J. Preparation of porous Si and TiO_2 nanofibres using a sulphur-templating method for lithium storage. *physica status solidi (a)* **2015,** *212* (4), 877-881.

34.   Wang, W.; Tian, M.; Wei, Y.; Lee, S.-H.; Lee, Y.-C.; Yang, R. Binder-free three-dimensional silicon/carbon nanowire networks for high performance lithium-ion battery anodes. *Nano Energy* **2013,** *2* (5), 943-950.

35.   Nadimpalli, S. P. V.; Sethuraman, V. A.; Dalavi, S.; Lucht, B.; Chon, M. J.; Shenoy, V. B.; Guduru, P. R. Quantifying capacity loss due to solid-electrolyte-interphase layer formation on silicon negative electrodes in lithium-ion batteries. *Journal of Power Sources* **2012,** *215*, 145-151.

36.   Lin, D.; Lu, Z.; Hsu, P.-C.; Lee, H. R.; Liu, N.; Zhao, J.; Wang, H.; Liu, C.; Cui, Y. A high tap density secondary silicon particle anode fabricated by scalable mechanical pressing for lithium-ion batteries. *Energy & Environmental Science* **2015,** *8* (8), 2371-2376.

37.   Wu, M.; Sabisch, J. E. C.; Song, X.; Minor, A. M.; Battaglia, V. S.; Liu, G. In Situ Formed Si Nanoparticle Network with Micron-Sized Si Particles for Lithium-Ion Battery Anodes. *Nano Letters* **2013,** *13* (11), 5397-5402.

38.   Wang, H.; Yang, Y.; Liang, Y.; Robinson, J. T.; Li, Y.; Jackson, A.; Cui, Y.; Dai, H. Graphene-Wrapped Sulfur Particles as a Rechargeable Lithium–Sulfur Battery Cathode Material with High Capacity and Cycling Stability. *Nano Letters* **2011,** *11* (7), 2644-2647.

39.   Ryu, H. S.; Guo, Z.; Ahn, H. J.; Cho, G. B.; Liu, H. Investigation of discharge reaction mechanism of lithium|liquid electrolyte|sulfur battery. *Journal of Power Sources* **2009,** *189* (2), 1179-1183.

40.   Fergus, J. W. Recent developments in cathode materials for lithium ion batteries. *Journal of Power Sources* **2010,** *195* (4), 939-954.

41.   Thongtem, T.; Thongtem, S. Characterization of $Li_{1-x}Ni_{1+x}O_2$ prepared using succinic acid as a complexing agent. *Inorganic Materials* **2006,** *42* (2), 202-209.

42.   Xu, Y.; Dunwell, M.; Fei, L.; Fu, E.; Lin, Q.; Patterson, B.; Yuan, B.; Deng, S.; Andersen, P.; Luo, H.; Zou, G. Two-Dimensional V_2O_5 Sheet Network as Electrode for Lithium-Ion Batteries. *ACS Applied Materials & Interfaces* **2014,** *6* (22), 20408-20413.

43.   Yang, Y.; Li, L.; Fei, H.; Peng, Z.; Ruan, G.; Tour, J. M. Graphene Nanoribbon/V_2O_5 Cathodes in Lithium-Ion Batteries. *ACS Applied Materials & Interfaces* **2014,** *6* (12), 9590-9594.

44.   Zhang, X.-F.; Wang, K.-X.; Wei, X.; Chen, J.-S. Carbon-Coated V_2O_5 Nanocrystals as High Performance Cathode Material for Lithium Ion Batteries. *Chemistry of Materials* **2011,** *23* (24), 5290-5292.

45.   Yan, J.; Sumboja, A.; Khoo, E.; Lee, P. S. V_2O_5 Loaded on SnO_2 Nanowires for High-Rate Li Ion Batteries. *Advanced Materials* **2011,** *23* (6), 746-750.

46.   Su, D.; Wang, G. Single-Crystalline Bilayered V_2O_5 Nanobelts for High-Capacity Sodium-Ion Batteries. *ACS Nano* **2013,** *7* (12), 11218-11226.

47.   Liu, F.; Song, S.; Xue, D.; Zhang, H. Selective crystallization with preferred lithium-ion storage capability of inorganic materials. *Nanoscale Research Letters* **2012,** *7* (1), 149.

48.   Chernova, N. A.; Roppolo, M.; Dillon, A. C.; Whittingham, M. S. Layered vanadium and molybdenum oxides: batteries and electrochromics. *Journal of Materials Chemistry* **2009,** *19* (17), 2526-2552.

49.   Song, T.; Xia, J.; Lee, J.-H.; Lee, D. H.; Kwon, M.-S.; Choi, J.-M.; Wu, J.; Doo, S. K.; Chang, H.; Park, W. I.; Zang, D. S.; Kim, H.; Huang, Y.; Hwang, K.-C.; Rogers, J. A.; Paik, U. Arrays of Sealed Silicon Nanotubes As Anodes for Lithium Ion Batteries. *Nano Letters* **2010,** *10* (5), 1710-1716.

50.   Sato, Y.; Nomura, T.; Tanaka, H.; Kobayakawa, K. Charge- Discharge Characteristics of Electrolytically Prepared V_2O_5 as a Cathode Active Material of Lithium Secondary Battery. *Journal of The Electrochemical Society* **1991,** *138* (9), L37-L39.

51.   Whittingham, M. S. Lithium Batteries and Cathode Materials. *Chemical Reviews* **2004,** *104* (10), 4271-4302.

52.   Chan, C. K.; Peng, H.; Twesten, R. D.; Jarausch, K.; Zhang, X. F.; Cui, Y. Fast, Completely Reversible Li Insertion in Vanadium Pentoxide Nanoribbons. *Nano Letters* **2007,** *7* (2), 490-495.

53.   Wu, H.; Qin, M.; Li, X.; Cao, Z.; Jia, B.; Zhang, Z.; Zhang, D.; Qu, X.; Volinsky, A. A. One step synthesis of vanadium pentoxide sheets as cathodes for lithium ion batteries. *Electrochimica Acta* **2016,** *206*, 301-306.

54.   Strathmann, H.; Kock, K.; Amar, P.; Baker, R. W. The formation mechanism of asymmetric membranes. *Desalination* **1975,** *16* (2), 179-203.

55.   Ying, C.; Jianxin, L.; Xiuwei, Z.; Yuzhong, Z. In-situ monitoring of polysulfone membrane formation via immersion precipitation using an ultrasonic through-transmission technique. *Desalination & Water Treatment* **2011,** *32* (1-3), 214-225.

56.   Kesting, R. E. *Synthetic polymeric membranes*. McGraw-Hill: New York, 1971.

57.   Greenlee, L. F.; Lawler, D. F.; Freeman, B. D.; Marrot, B.; Moulin, P. Reverse osmosis desalination: Water sources, technology, and today's challenges. *Water Research* **2009,** *43* (9), 2317-2348.

58.   Doménech-Carbó, M. T.; Aura-Castro, E. Evaluation of the Phase Inversion Process as an Application Method for Synthetic Polymers in Conservation Work. *Studies in Conservation* **1999,** *44* (1), 19-28.

59.   Saljoughi, E.; Sadrzadeh, M.; Mohammadi, T. Effect of preparation variables on morphology and pure water permeation flux through asymmetric cellulose acetate membranes. *Journal of Membrane Science* **2009,** *326* (2), 627-634.

60.   Liu, X. H.; Zhong, L.; Huang, S.; Mao, S. X.; Zhu, T.; Huang, J. Y. Size-Dependent Fracture of Silicon Nanoparticles During Lithiation. *ACS Nano* **2012,** *6* (2), 1522-1531.

61.   Eom, K.; Joshi, T.; Bordes, A.; Do, I.; Fuller, T. F. The design of a Li-ion full cell battery using a nano silicon and nano multi-layer graphene composite anode. *Journal of Power Sources* **2014,** *249*, 118-124.

62.   Klossek, A.; Mankovics, D.; Arguirov, T.; Ratzke, M.; Kirner, S.; Friedrich, F.; Gabriel, O.; Stannowski, B.; Schlatmann, R.; Kittler, M. Growth process of microcrystalline silicon studied by combined photoluminescence and Raman investigations. *Journal of Applied Physics* **2013,** *114* (22), 223511.

63.   Todica, M.; Stefan, T.; Simon, S.; Balasz, I.; Daraban, L. UV-Vis and XRD investigation of graphite-doped poly(acrylic) acid membranes. *Turkish Journal of Physics* **2014,** *38* (2), 261-267.

64.   Magasinski, A.; Dixon, P.; Hertzberg, B.; Kvit, A.; Ayala, J.; Yushin, G. High-performance lithium-ion anodes using a hierarchical bottom-up approach. *Nat Mater* **2010,** *9* (5), 461-461.

65.   Hatchard, T.; Dahn, J. In situ XRD and electrochemical study of the reaction of lithium with amorphous silicon. *Journal of The Electrochemical Society* **2004,** *151* (6), A838-A842.

66.   Li, J.; Dahn, J. R. An In Situ X-Ray Diffraction Study of the Reaction of Li with Crystalline Si. *Journal of The Electrochemical Society* **2007,** *154* (3), A156-A161.

67.   Obrovac, M. N.; Christensen, L. Structural Changes in Silicon Anodes during Lithium Insertion/Extraction. *Electrochemical and Solid-State Letters* **2004,** *7* (5), A93-A96.

68.   Beattie, S. D.; Loveridge, M. J.; Lain, M. J.; Ferrari, S.; Polzin, B. J.; Bhagat, R.; Dashwood, R. Understanding capacity fade in silicon based electrodes for lithium-ion batteries using three electrode cells and upper cut-off voltage studies. *Journal of Power Sources* **2016,** *302*, 426-430.

69.   Obrovac, M. N.; Christensen, L. Structural changes in silicon anodes during lithium insertion/extraction. *Electrochemical and Solid State Letters* **2004,** *7* (5), A93-A96.

70.   Dai, X.; Zhou, A.; Xu, J.; Lu, Y.; Wang, L.; Fan, C.; Li, J. Extending the High-Voltage Capacity of $LiCoO_2$ Cathode by Direct Coating of the Composite Electrode with Li_2CO_3 via Magnetron Sputtering. *The Journal of Physical Chemistry C* **2016,** *120* (1), 422-430.

71.   Mai, L.; Xu, L.; Han, C.; Xu, X.; Luo, Y.; Zhao, S.; Zhao, Y. Electrospun Ultralong Hierarchical Vanadium Oxide Nanowires with High Performance for Lithium Ion Batteries. *Nano Letters* **2010,** *10* (11), 4750-4755.

72.   Guillen, G. R.; Pan, Y.; Li, M.; Hoek, E. M. V. Preparation and Characterization of Membranes Formed by Nonsolvent Induced Phase Separation: A Review. *Industrial & Engineering Chemistry Research* **2011,** *50* (7), 3798-3817.

73.   Zhou, B.; He, D. Raman spectrum of vanadium pentoxide from density-functional perturbation theory. *Journal of Raman Spectroscopy* **2008,** *39* (10), 1475-1481.

74.   Mondal, T.; Bhowmick, A. K.; Krishnamoorti, R. Chlorophenyl pendant decorated graphene sheet as a potential antimicrobial agent: synthesis and characterization. *Journal of Materials Chemistry* **2012,** *22* (42), 22481-22487.

75.   Wu, J.; Huang, W.; Shi, Q.; Cai, J.; Zhao, D.; Zhang, Y.; Yan, J. Effect of annealing temperature on thermochromic properties of vanadium dioxide thin films deposited by organic sol–gel method. *Applied Surface Science* **2013,** *268*, 556-560.

76.   Cui, P.; Lee, J.; Hwang, E.; Lee, H. One-pot reduction of graphene oxide at subzero temperatures. *Chemical Communications* **2011,** *47* (45), 12370-12372.

77.   Nitta, N.; Wu, F.; Lee, J. T.; Yushin, G. Li-ion battery materials: present and future. *Materials Today* **2015,** *18* (5), 252-264.

78.   Li, J.; Daniel, C.; Wood, D. Materials processing for lithium-ion batteries. *Journal of Power Sources* **2011,** *196* (5), 2452-2460.